Received 21 June 2021; revised 5 November 2021; accepted 22 November 2021. Date of publication 24 November 2021; date of current version 9 December 2021. The review of this article was arranged by Associate Editor Shafiq Odhano.

Digital Object Identifier 10.1109/OJIA.2021.3130288

Impact Evaluation of Innovative Selective Harmonic Mitigation Algorithm for Cascaded H-Bridge Inverter on IPMSM Drive Application

G. SCHETTINO, C. NEVOLOSO, R. MICELI (Member, IEEE), A.O. DI TOMMASO, AND F. VIOLA (Member, IEEE)

Department of Engineering, University of Palermo, Viale delle Scienze, 90128 Palermo, Italy

CORRESPONDING AUTHOR: FABIO VIOLA (e-mail: fabio.viola@unipa.it)

This work was supported in part by the University of Palermo and in part by PON R&I 2015.2020 "Propulsione e Sistemi Ibridi per velivoli ad ala fissa e rotante.PROSIB", CUP no:B66C18000290005, in part by H2020-ECSEL-2017-1-IA-two-stage, in part by"first and european sic eightinches pilot line-REACTION", in part by Prin 2017- Settore/Ambito di intervento: PE7 linea C.Advanced power-trains and -systems for full electric aircrafts Prot. 2017MS9F49, in part by PON R&I 2014.2020.AIM (Attraction and International Mobility), project AIM1851228-1.

ABSTRACT This paper presents a detailed analysis of the use of a novel Harmonic Mitigation algorithm for Cascaded H-Bridge Multilevel Inverter in electrical drives for the transportation field. For this purpose, an enhanced mathematical model of Interior Permanent Magnet Synchronous Motor (IPMSM), that takes into account simultaneously saturation, cross-coupling, spatial harmonics, and iron loss effects, has been used. In detail, this model allows estimating accurately the efficiency and the torque ripple of the IPMSM, crucial parameters for transportation applications. Moreover, two traditional pulse width modulation strategies, Sinusoidal Phase-Shifted and Switching Frequency Optimal Phase-Shifted have been considered for comparison purposes with an optimized harmonic mitigation algorithm. Thus, this work provides a deep analysis of IPMSM drive performance fed by CHBMI, paying attention to various aspects such as the IPMSM efficiency, torque ripple, current, and voltage total harmonic distortion (THD). Finally, experimental investigations have been carried out to validate the analysis conducted.

INDEX TERMS Cascaded H-bridge multilevel inverter (CHBMI), efficiency, interior permanent magnet synchronous machine (IPMSM), selective harmonic mitigation algorithm, torque ripple.

I. INTRODUCTION

Multilevel inverters are a promising technology that results attractive for several kinds of applications such as medium voltage grid-connected PV systems[1]–[3], medium-high power transmission applications [4], medium-high power motor drives [5]–[7], and low-power low-voltage applications [8].

Compared to the traditional two-level inverters, multilevel converters present lower voltage stress, lower switching frequency, consequently smaller switching losses, lower *dv/dt*, and lower harmonic content in the output voltage waveforms. According to [9], the main multilevel inverter topological structures are Neutral-Point-Clamped Multilevel Inverter (NPCMI), Flying Capacitor Multilevel Inverter (FCMI), and Cascaded H-Bridges Multilevel Inverter (CHBMI). In particular, the CHBMI presents a modular structure, that allows easy expansion of the voltage levels by using fewer power devices concerning the other topology structures. Therefore, this topology can be successfully used in transportation applications such as automotive and aircraft where modular energy sources such as batteries and supercapacitors are employed. Indeed, the modularity feature allows improving the management and efficiency of the battery packages. Changing the point of view, there is also an improvement in terms of safety due to the voltage amplitude reduction of different levels of the converter.

In the transportation field, two key requirements are energy savings and the torque ripple that is the main source of noise and vibrations, as suggested in [10]–[11]. In this field, the permanent magnet synchronous machine (PMSM) is the most employed due to it is peculiar features such as high efficiency, high torque density, and wide operating speed range [12]–[14]. In literature, there are a huge amount of studies

concerning the benefits deriving by the use of multilevel inverters on PMSM electrical drives [15]–[19]. In detail, many control techniques have been proposed. The main control techniques discussed are direct torque control (DTC), model predictive control (MPC), and field-oriented control (FOC). The DTC presents the advantages of simplicity and robustness but presents the drawback of variable switching frequency and high torque ripple [15]–[16]. The MPC allows to obtain a very high dynamic performance but the implementation is complex and requires a large amount of calculation [17]–[18]. The FOC is a control technique where the electromagnetic torque and the air-gap flux control are carried out by controlling the stator currents amplitudes and their phase shift. However, the performances of the electric drive, are not only a function of the aforementioned control techniques but also of the modulation technique employed especially when a multilevel inverter is adopted [19]. The main control techniques and modulation strategies for multilevel inverters in traction applications have been discussed in [20]. More in detail, through a set of selection criteria based on traction systems requirements the control and modulation schemes, have been compared.

Regarding the modulation strategies, a large number of studies that analyze the benefits of the use of a multilevel converter, for different fields of applications, are reported in the literature [21], [22]. In high-power medium voltage applications, the device switching losses are predominant in respect of the conduction losses. Therefore, to obtain high converter efficiency, high device utilization, and reduced cooling requirements, the low-switching frequency modulation strategies such as Selective Harmonic Elimination (SHE) and Selective Harmonic Mitigation (SHM) algorithms have been adopted [23]–[24]. The SHE and SHM algorithms allow to eliminate or mitigate low-order voltage harmonics by using a set of non-linear transcendental equations system in which the order depends on the number of the voltage levels of the converter. Therefore, the evaluation of the control angles through the resolution of the non-linear transcendental equation system is the key issue of these methods. Thus, in literature, different approaches and innovative ways have been investigated to overcome and simplify the applications of SHE and SHM algorithms [25]–[29]. Regarding electrical drives fed by two-level inverters, different interesting studies focused on different aspects such as minimization of the torque ripple by using SHE algorithms [30]–[31] and the comparison of Space Vector and SHE PWM [32], are reported in the literature. From these studies, it is clear that performance can be improved by using multilevel technologies.

Other studies proposed the NPCMI topology structure as a conversion system for electrical drive applications. In particular, an interesting harmonic investigation by using a SHE-PWM for induction motor has been presented in [33]. In [34]–[35], a performance comparison between two-level and five-level NPCMI in electrical drive with FOC strategy and IPMSM motor has been presented, whereas five-level and seven-level NPCMI performances have been compared in [36]. In these studies, interesting results by using multilevel technology have been demonstrated. Nevertheless, the NPCMI has lower reliability due to the absence of modularity in the topology structure.

A five-level CHBMI topology structure for E-transportation has been proposed in [37], in which an interesting analysis that has taken into account state of charge, Total Harmonic Distortion (THD%), torque ripple, and switching losses has been carried out. Similar studies are reported in [38]–[39], where the performance of seven-level and nine-level CHBMI converters are presented, respectively. Although numerous studies about multilevel structures in different traction applications proposed them as a promising substitute, the worldwide markets have not used these topologies yet [20].

However, the scientific literature includes very few studies on the performance of PMSM electric drives fed by CHBMI with SHM modulation algorithms. Most of the studies focus the attention on PMSM electric drive performance by the use of Space Vector Pulse Width Modulation (SVPWM) both with traditional two-level inverters and with multilevel inverters [6], [15]–[16], [19], [32], [37]–[40]. For this reason, the main purpose of this work is to investigate the performance of IPMSM electric drives fed by five-level CHBMI with the SHM algorithm.

The goal of this work is to incentive the technological transition from traditional two-level inverters to multilevel technologies especially in the field of traction applications. For this purpose, this study investigates the performance of an electrical drive system in terms of overall efficiency and torque ripple through a detailed technical comparative analysis. In particular, this work has been carried out by using an enhanced mathematical model of an IPMSM to accurately estimate the motor losses (iron and copper losses) and torque ripple. In order to consider the impact on the system performances due to the multilevel converter employment, including the converter efficiency (switching and conduction losses), two PWM modulation strategies, commonly used in electrical drive applications, have been analyzed and compared. Moreover, the analysis has been completed by evaluating the IPMSM performance with FOC control by using an innovative harmonic mitigation algorithm. The current and voltage THD, obtained respectively with each modulation strategy, have been analyzed compared and discussed. Finally, the analysis carried out in the simulation environment has been validated with several experimental investigations on CHBMI and IPMSM prototypes that present the same features of CHBMI and IPMSM simulated.

This paper is organized into the following sections: Section II describes the considered electric drive system, compares the IPMSM finite element model with the enhanced mathematical model adopted for the study; Section III presents the conversion system based on the cascaded inverter topology, introduces two commonly used PWM techniques, the harmonic mitigation algorithm developed by authors in the previous work and the converter losses; Section IV describes objectives of the multiresolution performance analysis on IPMSM drive; Section V presents a discussion on the

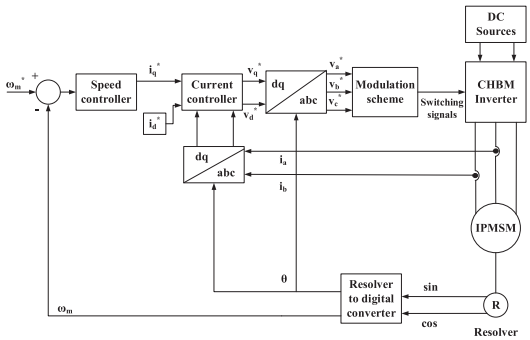

FIGURE 1. Field-oriented control block diagram of IPMSM drive system.

multiresolution study of the performances of IPMSM electric drive fed by the CHBMI by varying modulation strategies; finally, Section VI present the experimental analysis carried out.

II. ELECTRIC DRIVE SYSTEM

The FOC control strategy of the IPMSM drive fed by CHBMI is reported schematically in Fig. 1.

The control scheme presents a close-loop of the mechanical speed and close-loops of *dq*-axes current components. The speed and current errors are processed by PI controllers in order to obtain the reference *dq*-axis voltage values. Through inverse Park transformation, the reference *dq*-axis voltage components are reported in the three-phase reference frame and modulated by the modulation scheme block to obtain the switching signals for the CHBMI. The impact of the proposed SHM and the other modulation strategies on the IPMSM has been carried out in the Matlab/Simulink simulation environment. In detail, an enhanced mathematical model of IPMSM is considered for the accurate evaluation of torque ripple and efficiency. Below, it is described the IPMSM mathematical model adopted and the features of the IPMSM simulated.

A. IPMSM ENHANCED MATHEMATICAL MODEL

In literature, several studies propose an enhanced modelling approach of IPMSM [40]–[45]. A non-linear IPMSM mathematical model is defined and built by Xiao Chen et all in [40]–[41]. The modelling approach proposed the definition of the *dq*-axes flux linkage as a function of *dq*-axes currents and mechanical position to take into account the non-linear behavior of IPMSM and it is based on *dq*-axes currents versus *dq*-axes flux linkages inverse solution defined by look-up tables. An interesting comparative analysis of the proposed IPMSM modelling approach performance with respect to the experimental results is shown and discussed. In this modelling approach, the torque and voltage equations are not deeply investigated. In [42], the *dq*-axes flux linkages are defined as a function of the *dq*-axes currents and the temperature to improve the expression of the electromagnetic torque and detect more accurately the maximum torque per ampere trajectory of the IPMSM. In [44], the authors investigate the impact of harmonic components of MMF in the computation of the torque. Respect to the previous modelling approaches, the electromagnetic torque expression is computed by means coenergy approach and presents a torque component that is a function of the magnetic coenergy derivative with respect to the mechanical position. In [45], the authors present a modelling approach of IPMSM where the voltage equations are deeply investigated, discussed and the mathematical expression of electromagnetic torque obtained is similar with respect to described in [44]. The modelling approach is experimentally validated and predicts the electromagnetic behavior of the IPMSM but does not consider the iron losses and it cannot be used for accurate efficiency estimation of the machine.

In this study, an enhanced mathematical model of IPMSM, that considers saturation, cross-coupling, spatial harmonics, and iron loss effects, has been employed. In detail, the proposed mathematical model of IPMSM is defined starting from a previous study [46] where a mathematical model of IPMSM considering the saturation, cross-coupling, and spatial harmonics effects are described and discussed. This modelling approach is based on the definition of *dq*-axes flux linkage λ_d, λ_q as a function of *dq*-axes current components i_d, i_q, and mechanical position θ_m. The IPMSM voltage equations that take into account the saturation, cross-coupling, and spatial harmonics effects are:

$$\begin{aligned} v_d(t) = {} & Ri_d(t) + L_{dd}^{inc}\left(i_d, i_q, \theta_m\right) \cdot \frac{di_d}{dt} + L_{dq}^{inc}\left(i_d, i_q, \theta_m\right) \\ & \cdot \frac{di_q}{dt} + \frac{\partial \lambda_d\left(i_d, i_q, \theta_m\right)}{\partial \theta_m} \cdot \omega_m - \omega_e \\ & \times \left[L_q^{app}\left(i_d, i_q, \theta_m\right) \cdot i_q + \lambda_{qPM}\left(i_d, 0, \theta_m\right)\right] \end{aligned} \quad (1)$$

$$\begin{aligned} v_q(t) = {} & Ri_q(t) + L_{qd}^{inc}\left(i_d, i_q, \theta_m\right) \cdot \frac{di_d}{dt} + L_{qq}^{inc}\left(i_d, i_q, \theta_m\right) \\ & \cdot \frac{di_q}{dt} + \frac{\partial \lambda_q\left(i_d, i_q, \theta_m\right)}{\partial \theta_m} \cdot \omega_m + \omega_e \\ & \times \left[L_d^{app}\left(i_d, i_q, \theta_m\right) \cdot i_d + \lambda_{dPM}\left(0, i_q, \theta_m\right)\right] \end{aligned} \quad (2)$$

where v_d, v_q are the *dq*-axes voltage components, i_d, i_q are the *dq*-axes current components, ω_m is the mechanical angular speed, ω_e is the electrical angular speed, λ_{dPM}, λ_{qPM} are the *dq*-axes permanent magnet flux linkages, L_{ii}^{inc} and L_{ij}^{inc} represent the self and mutual incremental inductances components, L_d^{app} and L_q^{app} are the *dq*-axes non-coupled apparent inductances that including both self and cross-saturation effects [45]–[46]. Generally, the flux linkage λ_{qPM} can be neglected since it presents a very low value.

The electromagnetic torque is derived from the power relationship and its expression is defined by:

$$\begin{aligned} T_{em} = {} & \frac{3}{2} p\left[\lambda_d\left(i_d, i_q, \theta_m\right) \cdot i_q - \lambda_q\left(i_d, i_q, \theta_m\right) \cdot i_d\right] \\ & + \frac{3}{2}\left[\frac{\partial \lambda_d\left(i_d, i_q, \theta_m\right)}{\partial \theta_m} \cdot i_d + \frac{\partial \lambda_q\left(i_d, i_q, \theta_m\right)}{\partial \theta_m} \cdot i_q\right] \\ = {} & T_{em1} + T_{em2} \end{aligned} \quad (3)$$

$$T_{em1} = \frac{3}{2}p \cdot \left\{ \begin{array}{c} \left(\lambda_{dPM} \cdot i_q - \lambda_{qPM} \cdot i_d\right) \\ + \left[L_d^{app}\left(i_d, i_q, \theta_m\right) - L_q^{app}\left(i_d, i_q, \theta_m\right)\right] \cdot i_d \cdot i_q \end{array} \right\} \tag{4}$$

$$\begin{aligned} T_{em} &= \frac{3}{2}p\left[\lambda_d\left(i_d, i_q, \theta_m\right) \cdot i_q - \lambda_q\left(i_d, i_q, \theta_m\right) \cdot i_d\right] \\ &\quad + \frac{3}{2}\left[\frac{\partial \lambda_d\left(i_d, i_q, \theta_m\right)}{\partial \theta_m} \cdot i_d + \frac{\partial \lambda_q\left(i_d, i_q, \theta_m\right)}{\partial \theta_m} \cdot i_q\right] \\ &= T_{em1} + T_{em2} \end{aligned} \tag{5}$$

where T_{em1} represents the main torque component that contains the alignment torque and the reluctance torque components, whereas T_{em2} represents an additional ripple torque component.

For the analysis purpose of the CHBMI impact on the IPMSM performance, the IPMSM mathematical model has been improved considering the iron losses and the additional torque component function of the magnetic coenergy variation with the mechanical position. In detail, to evaluate the impact of the iron loss on electromagnetic behavior, the iron losses mathematical model described in [40] has been adopted. This modelling approach separates the iron losses into two loss components, one associated with the main magnetizing flux linkage and another one associated with the demagnetizing flux linkage that occurs during field weakening operations. This iron losses model tries to take into account the field weakening current effects that produce a stator reaction field component that opposes the main PM excitation field. Therefore, during the field weakening operations, the resultant flux linkage with the stator winding is thus reduced. The mathematical model is described by the following relationships:

$$\begin{aligned} p_{FE}^{OC} &= a_h \frac{E_m}{2\pi \lambda_{dPM}(0, i_q, \theta_m)} \\ &\quad + a_e\left(\frac{E_m}{2\pi \lambda_{dPM}(0, i_q, \theta_m)}\right)^2 + a_x\left(\frac{E_m}{2\pi \lambda_{dPM}(0, i_q, \theta_m)}\right)^{1.5} \end{aligned} \tag{6}$$

$$\begin{aligned} p_{FE}^{SC} &= b_h \frac{E_d}{2\pi \lambda_{dPM}(0, i_q, \theta_m)} \\ &\quad + b_e\left(\frac{E_d}{2\pi \lambda_{dPM}(0, i_q, \theta_m)}\right)^2 + b_x\left(\frac{E_d}{2\pi \lambda_{dPM}(0, i_q, \theta_m)}\right)^{1.5} \end{aligned} \tag{7}$$

where the iron loss coefficient (a_h, a_e, a_x) and (b_h, b_e, b_x) are the hysteresis, eddy current, and excess coefficients of the iron loss estimated by FEA open circuit simulations and of the iron loss estimated by FEA short circuit simulation, respectively. The total iron loss for a given IPMSM operating condition can be calculated as the sum of the two iron losses components. The expressions of the induced stator voltage E_m and of induced voltage due to the armature reaction of the d-axis current E_d are:

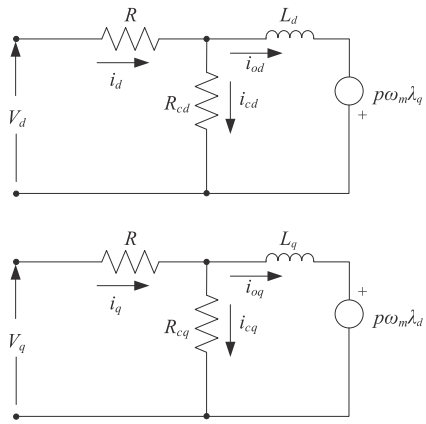

FIGURE 2. ***Dq*** **axes circuit models with iron loss components.**

$$E_m = 2\pi f\sqrt{\lambda_d^2\left(i_d, i_q, \theta_m\right) + \lambda_q^2\left(i_d, i_q, \theta_m\right)} \tag{8}$$

$$E_d = -2\pi f\left[\lambda_d\left(i_d, i_q, \theta_m\right) - \lambda_{dPM}\left(0, i_q, \theta_m\right)\right] \tag{9}$$

In order to take into account, the iron losses effects in the dq-axes modelling approach of IPMSM, it is possible to consider equivalent currents (i_{cd}, i_{cq}) that generate losses in equivalent fictitious resistors (R_{cd}, R_{cq}) positioned across the d- and q-axis induced voltages as shown in Fig 2.

For this purpose, the iron loss can be decomposed in the components associated with the dq-axes flux linkage, as expressed by:

$$p_{FE\_d} = \frac{\lambda_d^2}{\lambda_d^2 + \lambda_q^2} \cdot p_{FE}^{OC} + p_{FE}^{SC} \tag{10}$$

$$p_{FE\_q} = \frac{\lambda_q^2}{\lambda_d^2 + \lambda_q^2} \cdot p_{FE}^{OC} \tag{11}$$

The corresponding iron loss dq-axes currents components can be derived through the following relationships:

$$i_{cd} = \frac{p_{FE\_d}}{V_d - Ri_d} \tag{12}$$

$$i_{cq} = \frac{p_{FE\_q}}{V_q - Ri_q} \tag{13}$$

Therefore, below the relationships of the IPMSM enhanced mathematical model is described:

$$\begin{aligned} v_d(t) &= Ri_d(t) + L_{dd}^{inc}\left(i_d, i_q, \theta_m\right)\frac{di_{od}}{dt} + L_{dq}^{inc}\left(i_d, i_q, \theta_m\right)\frac{di_{oq}}{dt} \\ &\quad + \frac{\partial \lambda_d\left(i_d, i_q, \theta_m\right)}{\partial \theta_m}\omega_m - \omega_e\left[L_q^{app}\left(i_d, i_q, \theta_m\right) \cdot i_{oq} + \lambda_{qPM}\right] \end{aligned} \tag{14}$$

$$v_q(t) = Ri_q(t) + L_{qd}^{inc}\left(i_d, i_q, \theta_m\right)\frac{di_{od}}{dt} + L_{qq}^{inc}\left(i_d, i_q, \theta_m\right)\frac{di_{oq}}{dt}$$

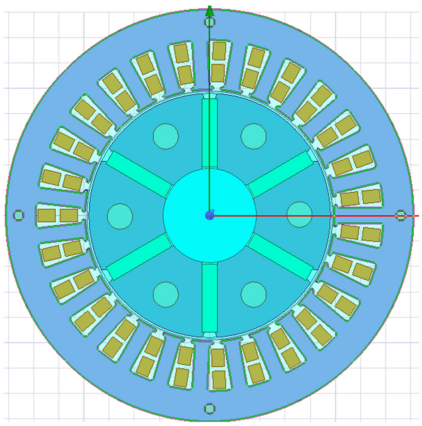

FIGURE 3. IPMSM cross section.

$$+\frac{\partial\lambda_d\left(i_d,i_q,\theta_m\right)}{\partial\theta_m}\omega_m-\omega_e\left[L_d^{app}\left(i_d,i_q,\theta_m\right)\cdot i_{od}+\lambda_{dPM}\right] \tag{15}$$

The torque expression has been improved including the magnetic energy variation with the mechanical position according to the magnetic coenergy approach described in [44]–[45]:

$$\begin{aligned}T_{em}=&\frac{3}{2}p\left[\lambda_d\left(i_d,i_q,\theta_m\right)\cdot i_{oq}-\lambda_q\left(i_d,i_q,\theta_m\right)\cdot i_{od}\right]\\&+\frac{3}{2}\left[\frac{\partial\lambda_d\left(i_d,i_q,\theta_m\right)}{\partial\theta_m}\cdot i_{od}+\frac{\partial\lambda_q\left(i_d,i_q,\theta_m\right)}{\partial\theta_m}\cdot i_{oq}\right]\\&-\frac{\partial W\left(i_d,i_q,\theta_m\right)}{\partial\theta_m}=T_{em1}+T_{em2}+T_{em3}\end{aligned} \tag{16}$$

where T_{em3} is correlated to the magnetic energy variation with mechanical position ($\partial W/\partial\vartheta_m$) and represents another torque ripple component and, with zero current excitation, it represents the cogging torque of IPMSM. Compared with equation (3), torque equation (16) contains more ripple components and can be used for more accurate detection of electromagnetic torque. The authors in [44]–[45] demonstrate the high fidelity of this torque modelling approach both with FEA and experimental results.

B. IPMSM UNDERSTUDY AND MATHEMATICAL MODEL VALIDATION

For the analysis purpose of the CHBMI impact on the IPMSM performance, a three-phase IPMSM with rotor tangentially magnetization is considered and simulated in FEA software. The cross-sectional view of the IPMSM is shown in Fig. 3 and the main electrical, mechanical and geometrical data are reported in Table I. The iron pack magnetic material is a 0.5 mm wide laminated sheet of type M330-50A, whereas the PMs are made by SMCo-18 MGOe whose B-H curves are shown in Fig. 4. In detail, the simulated IPMSM is a prototype present at the SDESLAB (Sustainable Development and Energy Saving Laboratory) of the University of Palermo

TABLE I Main Electrical and Mechanical Data of IPMSM

Quantity	Value
Power [kW]	0.8
Rated current [A]	3.6
Nominal Speed [rpm]	4000
Maximum Speed [rpm]	6000
Nr. of pole pairs	3
Nr. of phases	3
Nominal torque [Nm]	2
Peak torque [Nm]	9.2
Nr. of stator slot	27
Axial stator length [mm]	59
External stator diameter [mm]	81
Inner stator diameter [mm]	49.6
External rotor diameter [mm]	48
Inner rotor diameter [mm]	19

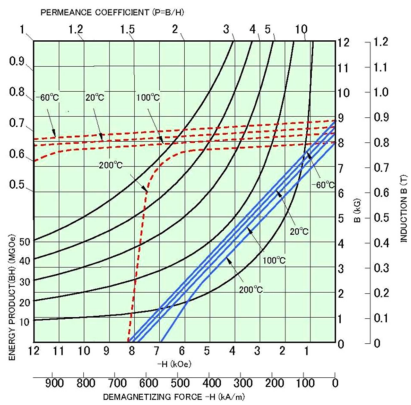

FIGURE 4. B-G curves of SMCo-18 MGOe PMs.

which will be shown subsequently in Section VI. Although the IPMSM analyzed is a low power machine, the results obtainable on this type of machine can also be extended to medium/high power IPMSM.

The electromagnetic quantities necessary for the use of the enhanced mathematical model of IPMSM, are obtained in *Ansys Maxwell* environment by 23250 magnetostatic simulations. In detail, each simulation is defined by fixing the dq-axes currents i_d, i_q, and electrical rotor position θ_e in the range [−7.5 A-7.5 A], [0 A-7.5 A] and [0°-360°], respectively. Negative values of the q-axis current i_q are not considered because only motor operations have been investigated. The derived electromagnetic quantities are shown and discussed in [46]. Furthermore, several transient simulations have been performed to determine the quantities necessary for the definition of the iron loss model.

The proposed IPMSM mathematical model has been implemented in Matlab/Simulink environment and its schematic diagram is reported in Fig. 5. Moreover, the mechanical equation has been included in the schematic representation where J is the inertia moment, T_L is the load torque and F is the viscous friction coefficient. All the

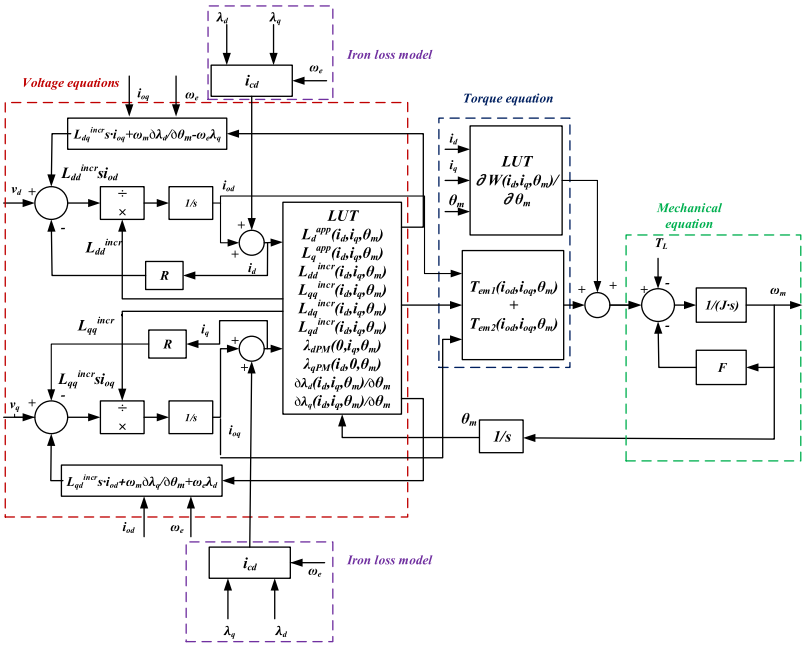

FIGURE 5. Schematic diagram of the proposed IPMSM mathematical model.

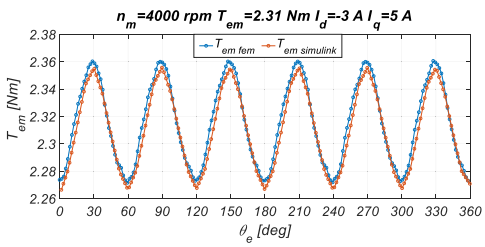

FIGURE 6. Torques comparison at 4000 rpm, 2.31 Nm.

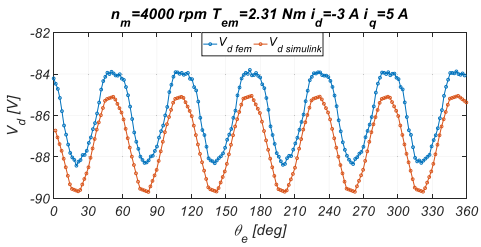

FIGURE 7. D-axis voltages comparison at 4000 rpm, 2.31 Nm.

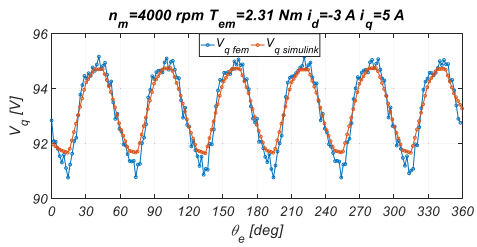

FIGURE 8. Q-axis voltages comparison at 4000 rpm, 2.31 Nm.

electromagnetic quantities of interest, such as the *dq*-axes non-coupled apparent inductances, the *dq*-axes incremental inductances, the *dq*-axes flux linkage produced by the PMs, the *dq*-axes flux linkages derivative terms, and magnetic energy derivative term, obtained by the characterization carried out in FEA environment, are implemented as lookup tables. A high number of representative operating points with different speed and load conditions have been investigated for validation purposes. In detail, a field-oriented control strategy has been adopted to drive the proposed IPMSM enhanced mathematical model for each working point of interest and the current waveforms are extracted and used as input quantities in the current FE model at the same speed condition.

In order to appreciate the benefits deriving by the proposed enhanced mathematical model of IPMSM, the same operating point analyzed in [46] has been considered, where the IPMSM operates at 4000 rpm, 2.31 Nm, and *d*- and *q*-axis current mean values equal to −3 A and 5 A. The comparison between the electromagnetic torque waveforms and the input *dq*-axes voltages waveforms predicted with the proposed Simulink model and the FE model are reported in Figs. 6–8. Compared to the results reported in [46], it is possible to detect a more accurate fidelity of the proposed enhanced mathematical model of IPMSM with respect to FEM results. Therefore, the proposed IPMSM enhanced mathematical model can be used to investigate the electromagnetic behavior of the IPMSM, especially in terms of efficiency and torque ripple and thus also the effectiveness of the new harmonic mitigation algorithm used to control the CHBMI.

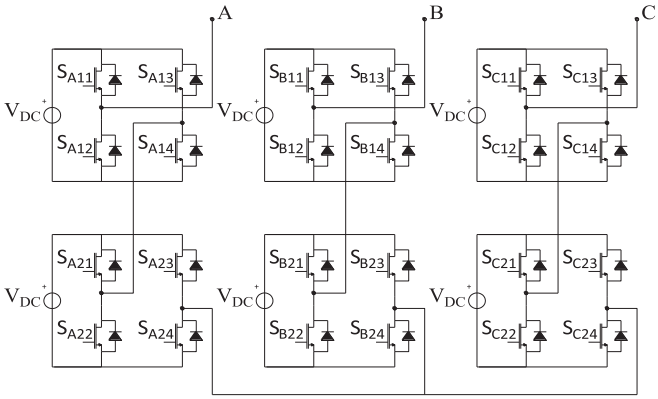

FIGURE 9. Tree-phase five-level CHBMI.

III. CONVERSION SYSTEM

In this section, the converter topology, the PWM modulation strategies, the harmonic mitigation algorithm, and the converter losses model have been described and discussed.

A. CONVERTER TOPOLOGY

This work aims to compare the performance of the IPMSM drive feds by a multilevel inverter. For this reason, in this subsection, the main features of the multilevel conversion system are discussed.

Traditional electrical drive systems are based on a three-phase Voltage Source Inverter (VSI). As well known, the VSI presents a simple topology structure with a single DC source. Nevertheless, this converter has several operative limits due to the power components technologies and high harmonic content on the output voltages. In terms of efficiency and torque ripple, these features generate performance degradation of the electrical drive systems. Multilevel power converters represent an innovation in the field of electrical drives for transportation applications. In particular, Cascaded H-Bridge Multilevel Inverter (CHBMI) thanks to their features (e.g. Modularity, low harmonic content, reduced voltage stress on the power components, and intrinsically fault-tolerant capability) are a promising solution. Fig. 9 shows a three-phase five-level CHBMI topology, starting from six different DC sources.

In respect of VSI, the three-phase five-level CHBMI presents a greater circuit complexity due to the high number of power components. In particular, it is composed of 2 H-Bridge modules in series connected for each phase. Thus, there are 24 power components S_{Xij} (phase $X=A\ldots C$; module $i=1\ldots 2$; and component $j=1\ldots 4$). Nevertheless, the modularity provides an intrinsic fault rejection in terms of continuity of operation, without adding other components, in respect to the other multilevel topology structures. Moreover, the separated DC sources allow improving the management and the efficiency of the battery packages on board in electrical vehicles, also by choosing the source that best suits the multilevel profile based on the state of charge.

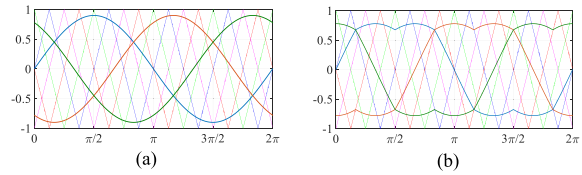

FIGURE 10 Modulation schemes: (a) Sinusoidal PS PWM and (b) SFO PS PWM for three-phase five-level CHBMI.

B. COMMON PWM MODULATION SCHEMES

Pulse Width Modulation (PWM) schemes are commonly used in different fields of applications due to their features (e.g. simple implementation in electronic devices and good response in terms of the harmonic content). Nevertheless, the PWM modulation schemes generate high-frequency voltage harmonics that increase the iron losses on the machine. To provide a complete analysis, the main PWM modulation schemes, adopted for three-phase five-level CHBMI, are discussed in this section.

Multicarrier PWM modulation schemes for multilevel converters represent an extension of the strategies for the two-level converter. Indeed, in literature are available several PWM modulation strategies based on the different dispositions of the triangular carrier signals like Level Shifted (LS) and Phase Shifted (PS), as discussed in [20] and [47]. In respect to the LS, the main feature of the PS is that the line-voltage harmonics are centered at a frequency f_h, defined as:

$$f_h = (m-1)\,k \cdot f_{PWM} \tag{17}$$

where f_{PWM} is the switching frequency, m is the number of the voltage levels, h is the harmonic order and k is an integer number. Moreover, the PS modulation schemes allow to control of each H-Bridge module as a single-phase converter and allow to uniform the power absorption for each DC source. For these reasons, the PS modulation schemes are chosen. In particular, the Sinusoidal PS PWM (Fig. 10a) and Switching Frequency Optimal (SFO) PS PWM (Fig. 10b) have been used in this work.

According to [48], the SFO modulation signals allow to obtain the same overall harmonic content of a Space Vector (SV) modulation PWM and it is possible to extend the range of the modulation index up to 1.15 inside the linear range. The SFO signals can be expressed as in (18) in which v_a, v_b and v_c are the traditional sinusoidal signals and v_{offset} is offset signal expressed as in (19).

$$\begin{cases} v_a^* = v_a - v_{offset} \\ v_b^* = v_b - v_{offset} \\ v_c^* = v_c - v_{offset} \end{cases} \tag{18}$$

$$v_{offset} = \frac{\max(v_a, v_b, v_c) + \min(v_a, v_b, v_c)}{2} \tag{19}$$

$$\hat{V}_{1,HM} = \frac{\sqrt{3}4V_{DC}}{\pi} \cdot [\cos(\alpha) + \cos(\beta)] \tag{20}$$

$$27\% < \hat{V}_{1,HM} < 46\%$$

$$\begin{cases} P_{\alpha 1} = -0.005283V_1^3 + 0.546467V_1^2 - 18.850946V_1 \\ \quad +303.954944 \\ P_{\beta 1} = +0.007458V_1^3 - 0.779991V_1^2 + 25.679520V_1 \\ \quad -213.613595 \end{cases}$$

$$46\% \leq \hat{V}_{1,HM} \leq 61\%$$

$$\begin{cases} P_{\alpha 2} = -0.937848V_1 + 119.636393 \\ P_{\beta 2} = -0.384619V_1 + 64.520958 \end{cases}$$

$$61\% < \hat{V}_{1,HM} \leq 80\%$$

$$\begin{cases} P_{\alpha 3} = -0.003094V_1^3 + 0.615244V_1^2 - 40.935430V_1 \\ \quad +971.599070 \\ P_{\beta 3} = +0.006572V_1^3 - 1.357658V_1^2 + 91.500486V_1 \\ \quad -1979.841849 \end{cases}$$

$$80\% < \hat{V}_{1,HM} \leq 97.5\%$$

$$\begin{cases} P_{\alpha 4} = -0.001483V_1^3 + 0.352683V_1^2 - 29.201203V_1 \\ \quad +888.028336 \\ P_{\beta 4} = -0.007426V_1^3 + 1.946315V_1^2 - 170.526122V_1 \\ \quad +5007.178491 \end{cases} \tag{21}$$

The main difference between SPS and SFOPS modulation schemes regards the amplitude of the first voltage harmonic that can be extended with SFO modulation signals. For a five-level converter, it is possible to evaluate the peak value of the first voltage harmonic, inside the linear region of the modulation index, by the expression:

$$\hat{V}_1 = 2MV_{DC} \tag{22}$$

where M is the modulation index and V_{DC} is the amplitude of the DC voltage equal supposed for each voltage level. Thus, it is evident an increase of the first voltage harmonic equal to 15% for modulation index equal to 1.15.

In terms of the overall voltage harmonics, both SPS and SFOPS present the same harmonics with a similar distribution in the magnitude spectra. By considering a switching frequency equal to 10 kHz, for a five-level converter, the first voltage harmonics are centered at 40 kHz both for SPS and SFOPS, according to equation (17). Thus, good response in terms of the current harmonic filter capability by the motor is expected. Moreover, thanks to this feature a lower torque ripple value is presumed.

Another interesting consideration regards the simple implementation in common electronic control unit devices. For a five-level converter, are necessary only four up-down digital counters to generate the carrier signals. Subsequently, in order to generate the gate signals are necessary twelve comparator circuits to compare modulation signals with carrier signals.

C. HARMONICS MITIGATION ALGORITHM

As described above, PWM modulation schemes introduce high voltage harmonics that generate a performance degradation in terms of the efficiency of the electrical drive.

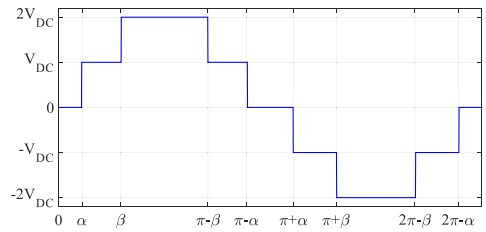

FIGURE 11. Staircase voltage pattern [29].

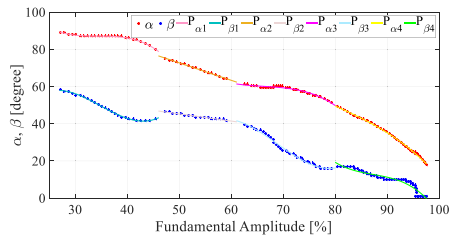

FIGURE 12. Approximation of the control angles trend in a range of the fundamental amplitude from 27% to 97.5% [29].

This phenomenon is greater in high-power electrical drive systems. The performance of the system can be improved by using low-switching modulation strategies, based on SHE or SHM algorithms specially designed for electrical drive applications. Nevertheless, the direct application of these algorithms presents high computational costs to evaluate the control angles.

According to [29], the authors have reduced computational costs and simplified the implementation by using an innovative Harmonic Mitigation (HM) algorithm to reduce fifth, seventh, and eleventh harmonics for three-phase five-level CHBMI, based on the traditional staircase voltage pattern (Fig. 11). In particular, by using an especially distortion index, it is possible to individuate control angle trends, called α and β, in the function of the fundamental amplitude (eq. 20) in a range from 27% to 97.5%. Subsequently, the control angle trends to control each level of the converter have been approximated by using low-order polynomial equations, as shown in Fig. 12. From the simulation analysis, it has been demonstrated that the control angles trends α and β have been approximated by using four low order polynomial equations (21). Through experimental tests, the effectiveness of the harmonic mitigation algorithm has been validated and compared with the simulation results by using Total Harmonic Distortion (THD), as shown in Fig. 13.

As described by the authors [29], the experimental tests have been carried out by using a FPGA-based control board (Altera Cyclone III). The HM algorithm overall execution time is 610 ns and, to generate the gate signals are necessary three up-down digital counters. Thus, it has been demonstrated that are not necessarily high hardware resources to implement the HM algorithm.

In terms of the harmonic content, the presence of low order voltage harmonics generates low order current harmonics that

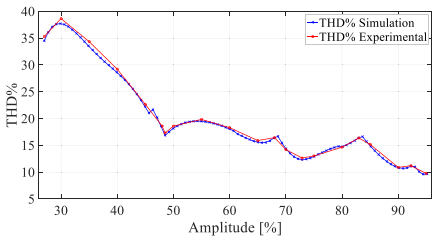

FIGURE 13. THD% comparison between simulation and experimental results [29].

TABLE II Maximum Values of the First Voltage Harmonics

SPS	SFOPS	HM
$\hat{V}_{1,\max} = 2V_{DC}$	$\hat{V}_{1,\max} = 2.3V_{DC}$	$\hat{V}_{1,\max} = 2.48V_{DC}$

cannot be filtered by the motor. For this reason, an increment of the torque ripple is expected. Anyhow, the absence of high-frequency harmonics should ensure a reduction in the iron losses in the motor.

Another difference, with respect to the SPS and SFOPS schemes, is about the DC power absorption. In this case, the DC power absorption is not uniform between the DC sources of a phase of the converter. Thus, in the design process of the DC sources, it is necessary to take into account this feature.

By using the HM algorithm, it is possible to increase the amplitude of the peak value of the first harmonic voltage, with respect to the SPS and SFOPS schemes. In Table II maximum values of the first harmonic voltage as a function of the amplitude of DC voltages, obtainable with SPS, SFOPS and HM algorithm, are reported.

As reported in Table II, it should be noted that the HM algorithm allows increasing the first voltage harmonics up to 24% with respect to the traditional SPS scheme.

D. CONVERTER LOSSES MODEL

In high-power electric drive applications, the efficiency of the converter system plays a key role. In particular, the converter losses can affect the overall efficiency of the system. The converter efficiency depends on the different variables as topology structure, modulation strategy, and power components technology.

By taking into account the topology structure of the H-Bridge module, depicted in Fig. 9, the current trends in each power component (e.g. mosfet) can be expressed in function of the current load and the switching states, as:

$$\begin{cases} i_{SA11} = [S_{A11} \wedge (S_{A14} \vee S_{A13})] \wedge (i_{Load} > 0) \\ i_{SA12} = [S_{A12} \wedge (S_{A13} \vee S_{A14})] \wedge (i_{Load} < 0) \\ i_{SA13} = [S_{A13} \wedge (S_{A11} \vee S_{A12})] \wedge (i_{Load} < 0) \\ i_{SA14} = [S_{A14} \wedge (S_{A11} \vee S_{A12})] \wedge (i_{Load} > 0) \end{cases} \tag{23}$$

where i_{SA1j} is the mosfet current (j=1...4), S_{A1j} is the generic switching state (called with the same name of the corresponding power component) and i_{Load} is the current load. Similarly, the diode currents are expressed as:

$$\begin{cases} i_{DA11} = (S_{A11} \wedge S_{A13}) \wedge (i_{Load} < 0) \\ i_{DA12} = (S_{A12} \wedge S_{A14}) \wedge (i_{Load} > 0) \\ i_{DA13} = (S_{A13} \wedge S_{A11}) \wedge (i_{Load} > 0) \\ i_{DA14} = (S_{A14} \wedge S_{A12}) \wedge (i_{Load} < 0) \end{cases} \tag{24}$$

where i_{DA1j} is the diode current. Thus, by using the current trends (23) and (24) of each power component the conduction losses and the switching losses have been estimated by using the datasheet parameters.

The conduction losses in the power mosfets $P_{cond(mos)}$ have been estimated by considering the Drain-Source On-state Resistance $R_{DS(ON)}$, expressed as:

$$P_{cond(mos)} = \frac{1}{T}\int_0^T R_{DS(ON)} i_{Sij}^2(t)\,dt \tag{25}$$

where T is the period of the fundamental amplitude of the current and i_{Sij} is the current mosfet. The conduction losses of the body-diode $P_{cond(diode)}$ have been estimated by considering the diode forward voltage V_{SD}, expressed as:

$$P_{cond(diode)} = \frac{1}{T}\int_0^T V_{DS} i_{Dij}(t)\,dt \tag{26}$$

where i_{Dij} is the diode current.

The MOSFET switching losses P_{sw} have been estimated by considering turn-on delay time $t_{d(ON)}$, rise-time t_r, turn-off delay time $t_{d(OFF)}$, and fall-time t_f. Thus, the switching losses are expressed as:

$$P_{sw} = \frac{1}{T}\sum_{k=1}^{N} V_{dc}\left[i_{kSij(On)} t_{On} + i_{kSij(Off)} t_{Off}\right] \tag{27}$$

where k is the k-th commutation, N is the number of commutations in a period of the fundamental current, $i_{kSij(on)}$ is the instantaneous load current through the switch in a turn-on, $i_{kSij(off)}$ is the instantaneous load current through the switch in turn-off, t_{on} is the overall turn-on time ($t_{d(On)}$+t_r) and t_{Off} is the overall turn-off time ($t_{d(Off)}$+t_f).

The overall losses of the converter can be estimated by considering the contribution of all H-Bridge modules.

In the next section, a brief description and the mathematical expressions of the tools, used in this work for the analysis purpose, have been reported.

IV. ANALYSIS TOOLS OF IPMSM DRIVE PERFORMANCE

As described above, the main purpose of this work is to investigate the overall performances of IPMSM electric drives fed by five-level CHBMI. In particular, the analysis has been focused on the performance comparison among PWM modulation strategies, SPS and SFO PS, and the harmonic mitigation algorithm, previously discussed in Section III.

Thanks to the advanced mathematical model, described in Section II, the analysis has been carried out by considering the following quantities:

- Power losses (P_{tot});
- Efficiency ($\eta_{\%}$);
- Torque ripple ($T_{ripple\%}$);
- Torque harmonics components ($T_h\%$);
- Voltages and currents harmonics.

In the overall power losses, the copper losses P_{cu} and iron-losses P_{fe} components have been considered, as:

$$P_{tot} = P_{cu} + P_{fe} \tag{28}$$

As well known, the power converters are harmonics generators. Thus, the presence of harmonics in the electric quantities generates additional losses with respect to the sinusoidal supply. The IPMSM mathematical model adopted allows evaluating accurately the contribution of current and voltage harmonic components not only on the electromagnetic torque but also on copper and iron losses components. In detail, to consider the contributions of the different harmonic components, the instantaneous trends of copper and iron losses have been investigated and the average values of the copper and iron losses, in a period of the fundamental current, have been evaluated as:

$$P_{cu} = \frac{1}{T}\int_0^T p_{cu}(t)dt \tag{29}$$

$$P_{cu} = P_{cu(h=0)} + \sqrt{\frac{1}{2}\cdot\left(\sum_{h=1}^{N} P_{hcu}^2\right)} \tag{30}$$

where $p_{cu}(t)$ and $p_{fe}(t)$ are the instantaneous values of the copper and iron losses, respectively.

The overall efficiency of the system has been evaluated in percent as:

$$\eta_{\%} = \frac{P_m}{P_m + P_{cu} + P_{fe} + P_{conv}}\cdot 100 \tag{31}$$

where P_{conv} is the overall converter losses, P_m is the mechanical power calculated starting electromagnetic torque T_{em} and speed ω_m values, as:

$$P_m = T_{em}\cdot\omega_m. \tag{32}$$

The torque ripple T_{ripple} has been evaluated as:

$$T_{ripple} = \frac{\max(T_{em}) - \min(T_{em})}{T_{avg}}\cdot 100 \tag{33}$$

where T_{avg} is the average torque value. Furthermore, the electromagnetic torque T_{em} can be decoupled into the dc and harmonics components:

$$T_{em} = T_{avg} + \sum_h T_{emh}\cos(h\theta - \varphi_h) \tag{34}$$

where T_{emh} represents the amplitude of hth harmonic component and φ_k represents the phase angle of hth harmonic component. Therefore, the main torque harmonic components T_{emh} have been investigated and compared for further analysis, expressed in percent of the torque average value (35).

$$T_h\% = \frac{T_h}{T_{avg}}\cdot 100 \tag{35}$$

The used tool to compare the harmonic components in voltages and currents is the Total harmonic Distortion – THD, expressed as:

$$THD\% = \sqrt{\frac{V_{rms}^2 - V_{rms,1}^2}{V_{rms,1}^2}}\cdot 100 \tag{36}$$

where V_{rms} is the root mean square value of the voltage (or current) and $V_{rms,1}$ is the root mean square value of the first-harmonic of the voltage (or current).

TABLE III DC Voltage Amplitudes

Topology structure	Modulation strategies	DC voltage [V]
Three-phase five-level CHBMI	SPS PWM	75 (for each voltage level)
	SFOPS PWM	65 (for each voltage level)
	SHM algorithm	60 (for each voltage level)

V. IPMSM DRIVE PERFORMANCE WITH HM ALGORITHM

This section aims to present the results obtained in this work. The analysis has been carried out in different conditions in terms of speed and load torque. In particular, the speed has changed in a range from 1500 rpm to 4000 rpm, while the load torque has been changed in the range from 0.5 Nm to 2 Nm.

To optimize the DC voltage utilization, in order to work inside the linear region of the modulation index, the DC voltage amplitudes have been chosen by considering the features of each modulation strategy. In this way, the DC voltage amplitudes used in this analysis are summarized in Table III. It is interesting to note that the voltage amplitudes are different for each modulation strategy considered. This result highlights the importance of the modulation technique in the design of the battery pack in electrical vehicle applications.

For the converter efficiency evaluation, the authors considered the power component parameters of a three-phase five-level CHBMI prototype, present at the SDESLAB of the University of Palermo, that is experimentally tested in previous works [29], [47] and which will be shown subsequently in Section VI. In particular, the main features of the power components are summarized in Table IV.

The following results have been obtained through simulation analysis in MATLAB/Simulink environment in which the advanced mathematical model, presented in Section II, and the mathematical model of a five-level three-phase CHBMI have been implemented.

TABLE IV Power Components Parameters

Productor	International Rectifier
Drain-Source Voltage - V_{DS}	150 V
Continuous Drain current - I_D	104 A
Static Drain-to-source On-Resistance $R_{DS(ON)}$	9.3 mΩ
Turn-On Delay Time $t_{d(on)}$	18 ns
Rise Time t_r	73 ns
Turn-Off Delay Time $t_{d(off)}$	41 ns
Fall Time - t_f	39 ns

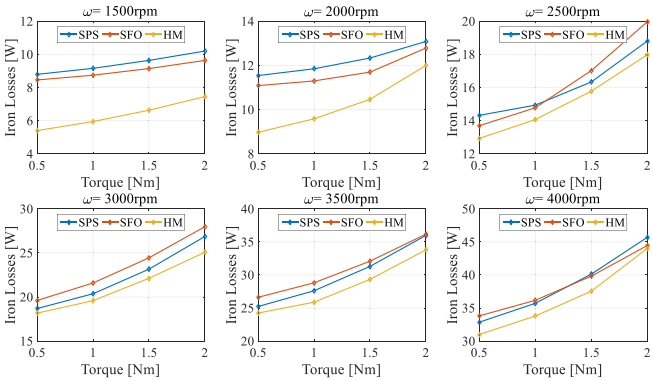

FIGURE 14. Comparison of iron losses trends.

As previously described, in the first step the analysis has been focused on the evaluation of the iron-losses, copper-losses, and the overall efficiency. In all figures, the blue curves are the results obtained with the SPS algorithm, the red curves are the results obtained with the SFO PS algorithm and the yellow curves are the results obtained with the HM algorithm.

Fig. 14 shows the iron-losses trends evaluated for each value of speed and load-torque considered. It is interesting to note that in each case the lower iron losses have been obtained with the HM algorithm. This result confirms the benefits introduced by the HM algorithm thanks to the lower harmonic components in the voltages. Also, it is interesting the behavior of the iron-losses trends obtained with SPS and SFOPS schemes. In particular, for lower values of speed, from 1500 rpm to 2000 rpm, the worst results have been obtained with the SPS modulation scheme. From 3000 rpm to 3500rpm of speed, the worst results have been obtained with SFOPS. Instead, the results are similar between SPS and SFO PS for 2500 and 4000 rpm of speed.

Fig. 15 shows the power copper-losses for each mechanical (speed and torque) condition considered. As well known, the copper losses are mainly generated by the fundamental components of the current that allows the generation of the average torque. Indeed, in all cases, copper loss trends are overlapped for each modulation schemes taken into account.

Fig. 16 shows the converter losses trend in which emerged the benefit introduced by the HM algorithm. In particular, it is interesting to note that the differences, between PWM schemes and the HM algorithm, increase with the speed. This result can be explained by studying the current distribution

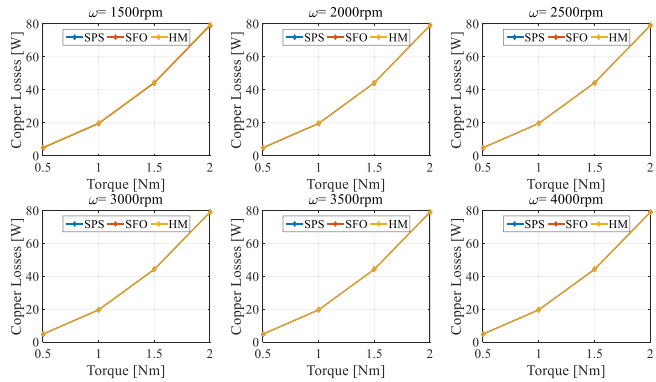

FIGURE 15. Comparison of copper losses trends.

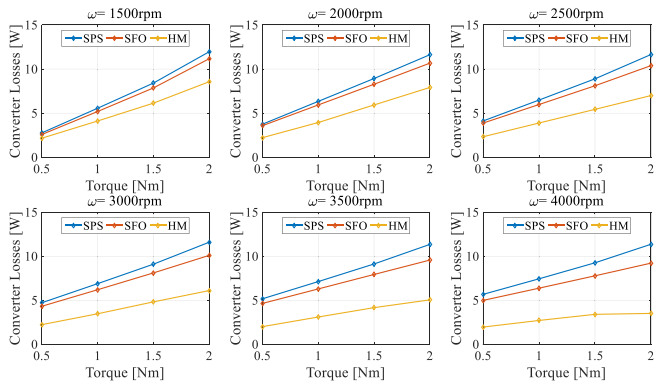

FIGURE 16. Comparison of the converter losses.

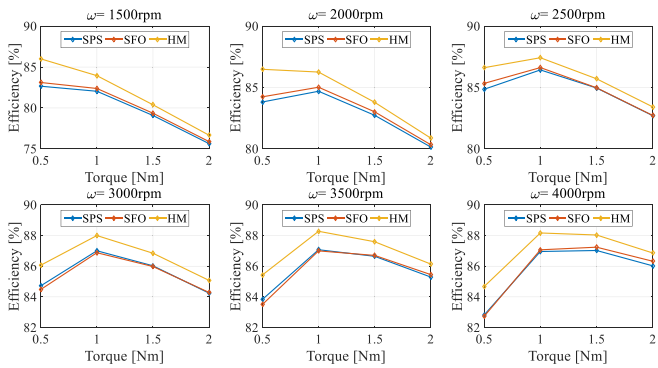

FIGURE 17. Comparison of overall efficiency trends.

among the power components in the H-Bridge as a function of the control angles trend shown in Fig. 12. In particular, in the H-Bridge modules driven with α control angle, the conduction losses of the body diode are predominant in respect to the conduction losses of the MOSFET. By increasing the speed, the contribution of the body diode conduction losses is reduced generating a reduction in the overall converter losses.

Although the copper losses represent the predominant contribution in the IPMSM efficiency, the reduction of the iron losses and the converter losses, produced by the HM algorithm, increases the overall efficiency of the IPMSM, as shown in Fig. 17. The efficiency improvement detected, due

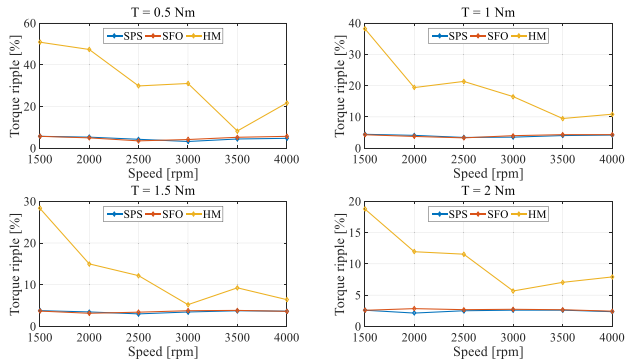

FIGURE 18. Comparison of torque ripple trends.

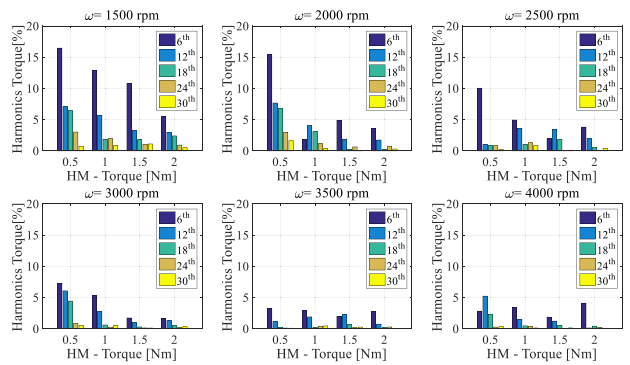

FIGURE 19. Main harmonics torque with HM algorithm.

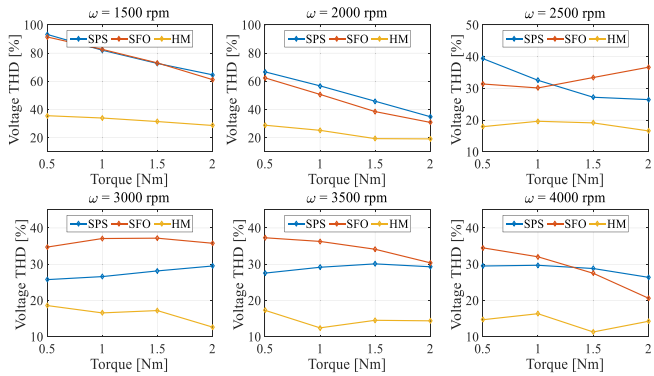

FIGURE 20. Comparison of voltage THD%.

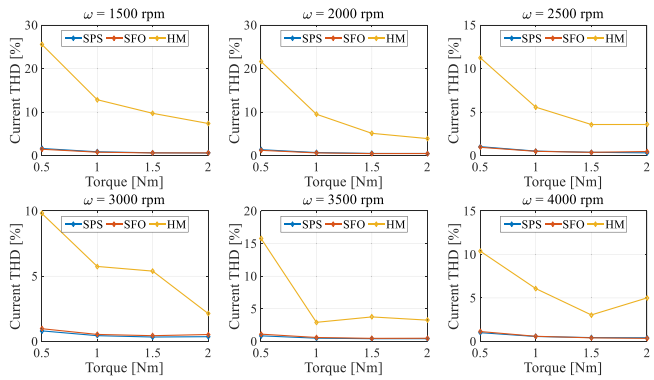

FIGURE 21. Comparison of current THD%.

to the HM algorithm, is on average similar in all speed-torque conditions considered. In detail, for the low power system considered in this work, efficiency gains of up to 2% have been obtained. Thus, greater efficiency results are expected for high power electrical drive systems.

As described above, thanks to the advanced model of IPMSM, a detailed analysis of the electromagnetic torque was carried out. Fig. 18 shows the torque ripple trends for each condition considered. The torque ripple is the result of electromagnetic interaction of different sources, especially, the harmonics in the magnet flux, the cogging torque, and current harmonics due to inverter nonlinearity. In terms of the torque ripple, the HM algorithm presents the highest values among the modulation schemes considered.

More in detail, the torque ripple is due to the presence of low-order harmonics in the torque, as shown in Fig. 19 for the HM algorithm. From the harmonic analysis on the torque is emerged that the odd-harmonics in the current generate harmonics in the torque but of even-order. In particular, it is possible to demonstrate that each torque harmonic order h multiples of six results from the electromagnetic interaction of the odd-harmonics $h\pm1$ in the currents, as shown in Fig. 22, with the permanent magnet flux and the machine anisotropy [49]. For example, the 6th torque harmonic is generated from the presence of the 5th and 7th current harmonics. Nevertheless, good harmonic mitigation of the torque harmonics has been obtained for high values of the speed and load torque. Moreover, there are some operation points where the torque ripple is similar and in particular, the differences are lower for higher values of the speed and load torque. Therefore, from these results, it is possible to claim that the HM algorithm introduces interesting benefits in terms of efficiency although with an increase in the torque ripple values for low speed and load torque values.

The performance of the system has been analyzed by comparing the THD% among the voltage and currents for further studies.

Figs. 20 and 21 show the comparison of THD%, among SPS, SFOPS, and HM, of voltages and currents, respectively. It should be noted that the HM algorithm allows obtaining the lower values of THD% in the voltage. Instead, in terms of the THD% in the currents, the worst results have been obtained with the HM algorithm. Nevertheless, the THD% trend of the current decreases for high speed and torque values.

VI. EXPERIMENTAL ANALYSIS

In order to validate the analysis carried out in the Matlab/Simulink environment, several experimental investigations have been conducted. For this purpose, a three-phase five-level CHBMI prototype composed of six power H-bridges MOSFET-based, whose technical data are the same as simulation analysis (Table IV), has been used. The experimental investigations are focused both on CHBMI performance

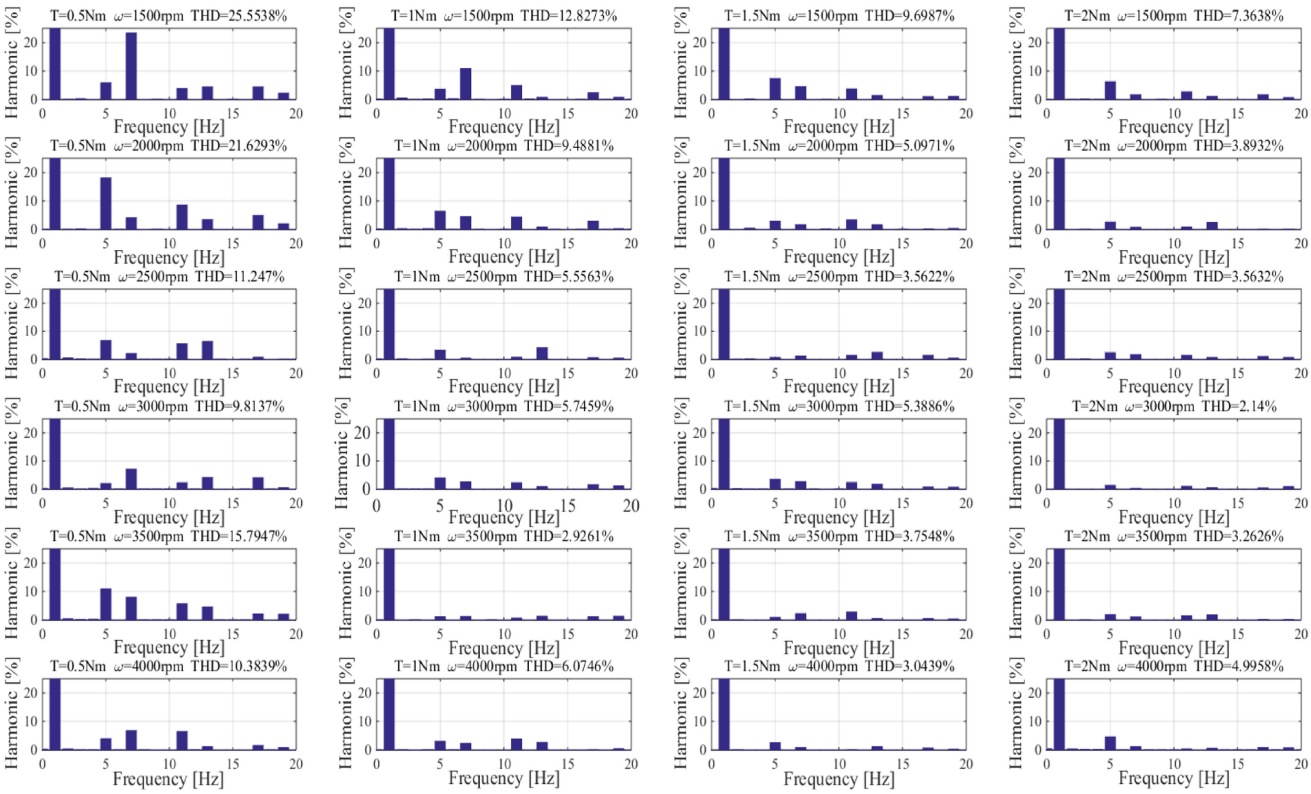

FIGURE 22. Current harmonic components with HM algorithm.

and both on electrical drive performance when each modulation control strategy, previously discussed, is employed. In this regard, an experimental analysis of the CHBMI performance when supplying a passive load is first presented below, followed by the experimental analysis of the electric drive performance equipped with an IPMSM prototype.

A. CHBMI PERFORMANCE WITH PASSIVE THREE-PHASE LOAD

The experimental analysis has been carried out on a laboratory test bench, shown in Fig. 23.

In detail, the control modulation strategies have been implemented on a prototype of FPGA-based (Altera Cyclone III) control board where the mathematical operations are managed by a digital clock signal with a frequency equal to 100 MHz. Each CHBMI H-bridge is powered by DC RSP-2400 sources with 48 V of rated voltage and the CHBMI supply a three-phase passive RL load with resistance R=20 Ω and inductance L=3 mH. The CHBMI input power is measured by two Yokogawa power meters model WT130 and WT330, respectively. The CHBMI voltage and current output quantities are sensed by the use of two Yokogawa 700924 voltage differential probes and the use of two Yokogawa 701933 current probes, respectively. Moreover, these electrical quantities are acquired by the use of the Teledyne LeCroy WaveRunner 640Zi oscilloscope with a sampling frequency equal to 10 MS/s. This choice is fundamental for accurate analysis in the frequency domain of electrical quantities and

FIGURE 23. Test bench with passive three-phase load.

accurate CHBMI output power measurement. The CHBMI performance in terms of THD, power losses and efficiency have been investigated for different values of fundamental harmonic voltage frequency equal to 50 Hz, 100 Hz, 150 Hz and 200 Hz and for fixed switching frequency value equal to 10 kHz.

Fig. 24 shows the voltage THD% trend of the CHBMI as a function of fundamental harmonic voltage amplitude obtained with each modulation strategy. As expected, the best CHBMI

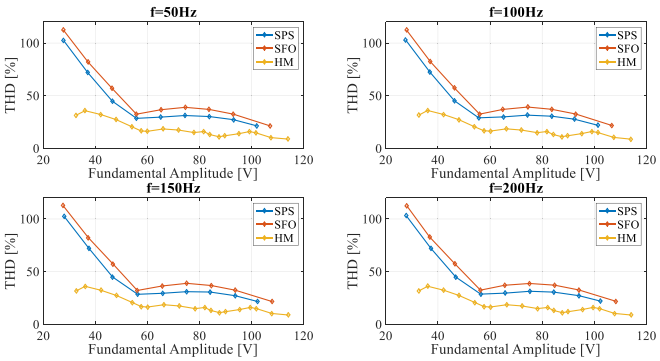

FIGURE 24. Experimental comparison of voltage THD%.

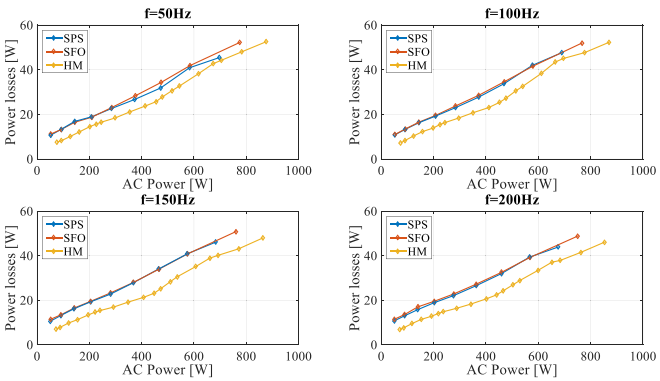

FIGURE 25. Experimental comparison of CHBMI power losses.

performances in terms of THD% are obtained with HM modulation strategy validating the results obtained in simulation analysis. Moreover, the experimental investigations highlight that the CHBMI performance in terms of harmonic content is not a function of fundamental voltage frequency for each modulation strategy and, therefore, the THD values is pretty much similar for fixed fundamental voltage amplitude.

Fig. 25 shows the trend of CHBMI power losses as a function of output AC power obtained with each modulation strategy. Also in this analysis, an improvement of CHBMI performance in terms of power losses reduction has been detected with the use of the HM control strategy. These power losses reductions result in an improvement of the CHBMI efficiency that is shown in Fig. 26. In detail, a significant improvement of CHBMI efficiency is obtained for low values of AC output power. Instead, for higher values of AC output power, the CHBMI efficiency obtained with HM modulation strategy is about 1-2% higher with respect to the CHBMI efficiency obtained with the other two modulation strategy considered.

B. IPMSM DRIVE PERFORMANCE FED BY CHBMI

The experimental investigations have been carried out on a three-phase IPMSM with rotor tangentially magnetization that presents the same electrical and mechanical features of IPMSM simulated (Table I). The IPMSM prototype is controlled by the FOC strategy, described in Section II and shown

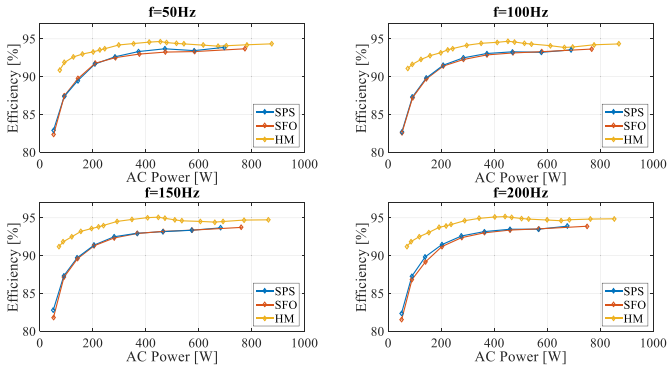

FIGURE 26. Experimental comparison of CHBMI efficiency.

TABLE V Peak Values of the Phase Volatges

SPS	SFOPS	HM
$\hat{V}_{1,\max} = 96V$	$\hat{V}_{1,\max} = 110.4V$	$\hat{V}_{1,\max} = 119.04V$

in Fig. 1. The test bench set-up is the same employed for CHBMI performance analysis and it is shown in Fig. 27. The IPMSM shaft is connected to a Magtrol hysteresis brake (Model HD-715-8NA) which is used as mechanical load. The hysteresis brake can be programmed in real-time by the dynamometer Magtrol DSP 6001 which allows the application of several torque load values.

The IPMSM drive performance have been investigated for several working points defined in terms of mechanical speed and load torque. For the investigation purpose, five mechanical speed values from 1500 rpm to 3500 rpm with a step of 500 rpm and four load torque from 0.5 Nm to 2 Nm with a step of 0.5 Nm have been considered, respectively. The working points defined are the same as those considered for the investigations carried out in simulation except the working points at 4000 rpm. These working points have been excluded from the experimental investigations because IPMSM operations at 4000 rpm result in CHBMI overmodulation operations when the SPS modulation technique is used. Therefore, the IPMSM drive performance obtained with the SPS modulation technique can not be compared with those obtained with the other two modulation techniques at 4000 rpm. Indeed, the maximum voltage amplitude (peak value) obtainable with SPS scheme, with a DC voltage amplitude equal to 48 V for each voltage level, is lower than the rated voltage of the motor (110 V peak value at 4000 rpm), as reported in Table V. Over these values, the converter works in overmodulation region.

Since the CHBMI performance have been analyzed in the previous section with a passive RL load, the comparative performance analysis is focused on IPMSM performance and overall drive performance. In detail, in Fig. 28 and Fig. 29 the motor efficiency trends and overall drive efficiency trends as a function of mechanical speed for each load torque value are reported, respectively.

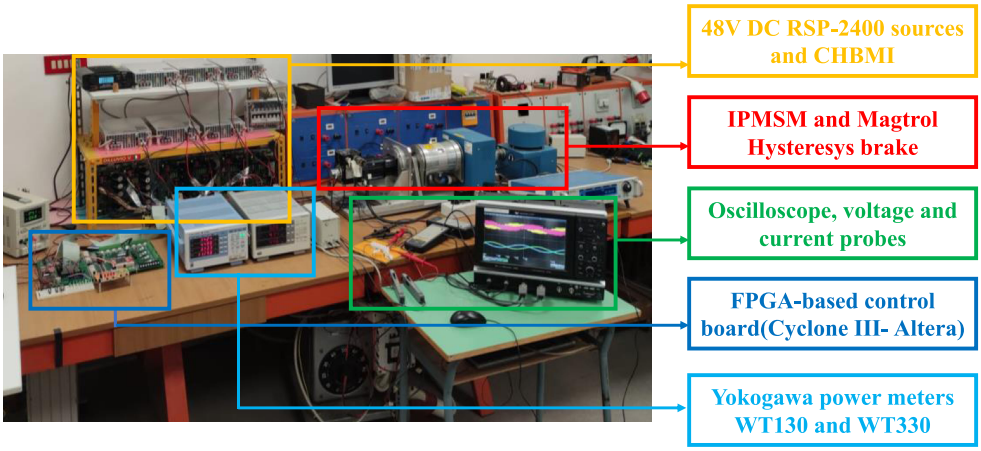

FIGURE 27. Test bench of IPMSM drive fed by CHBMI.

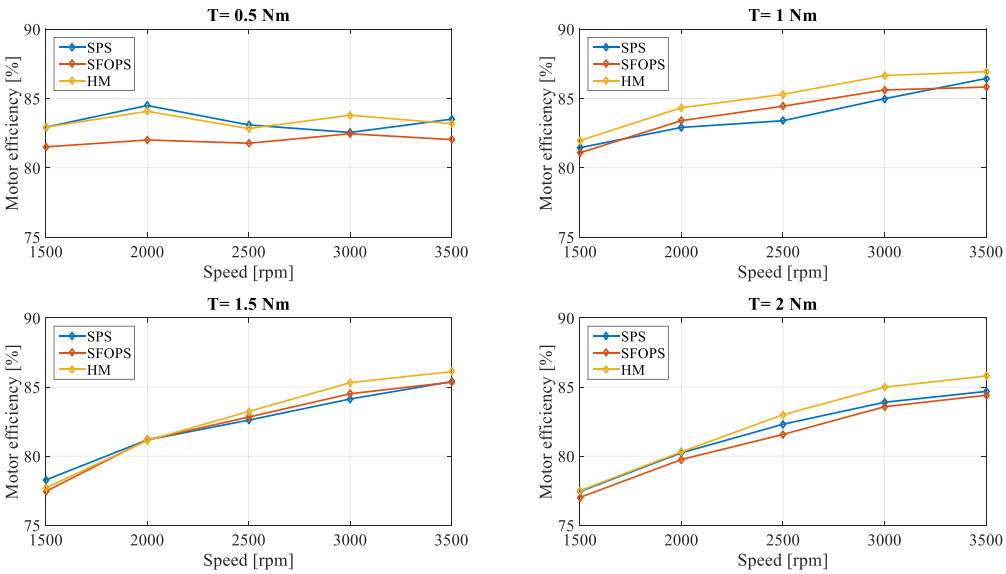

FIGURE 28. Experimental comparison of motor efficiency trends.

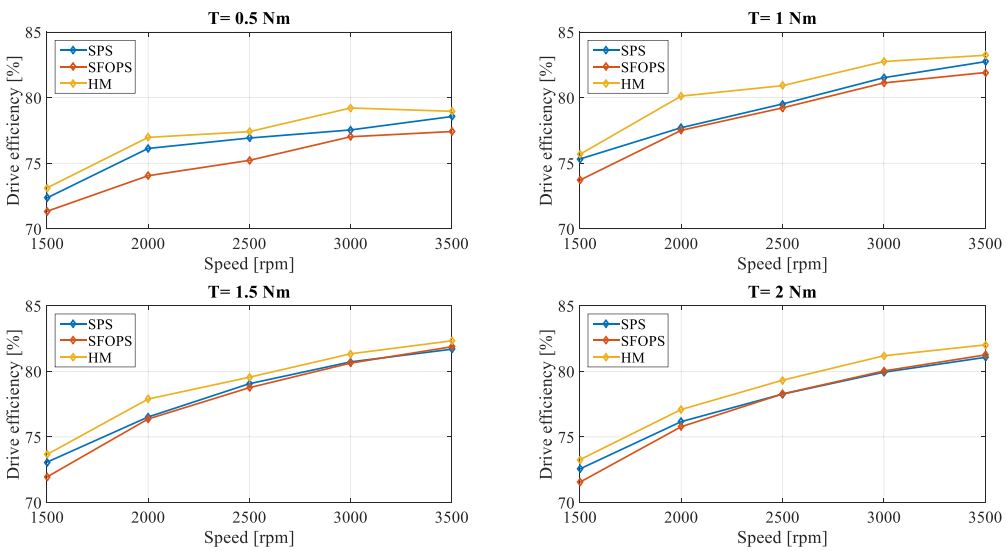

FIGURE 29. Experimental comparison of overall drive efficiency trends.

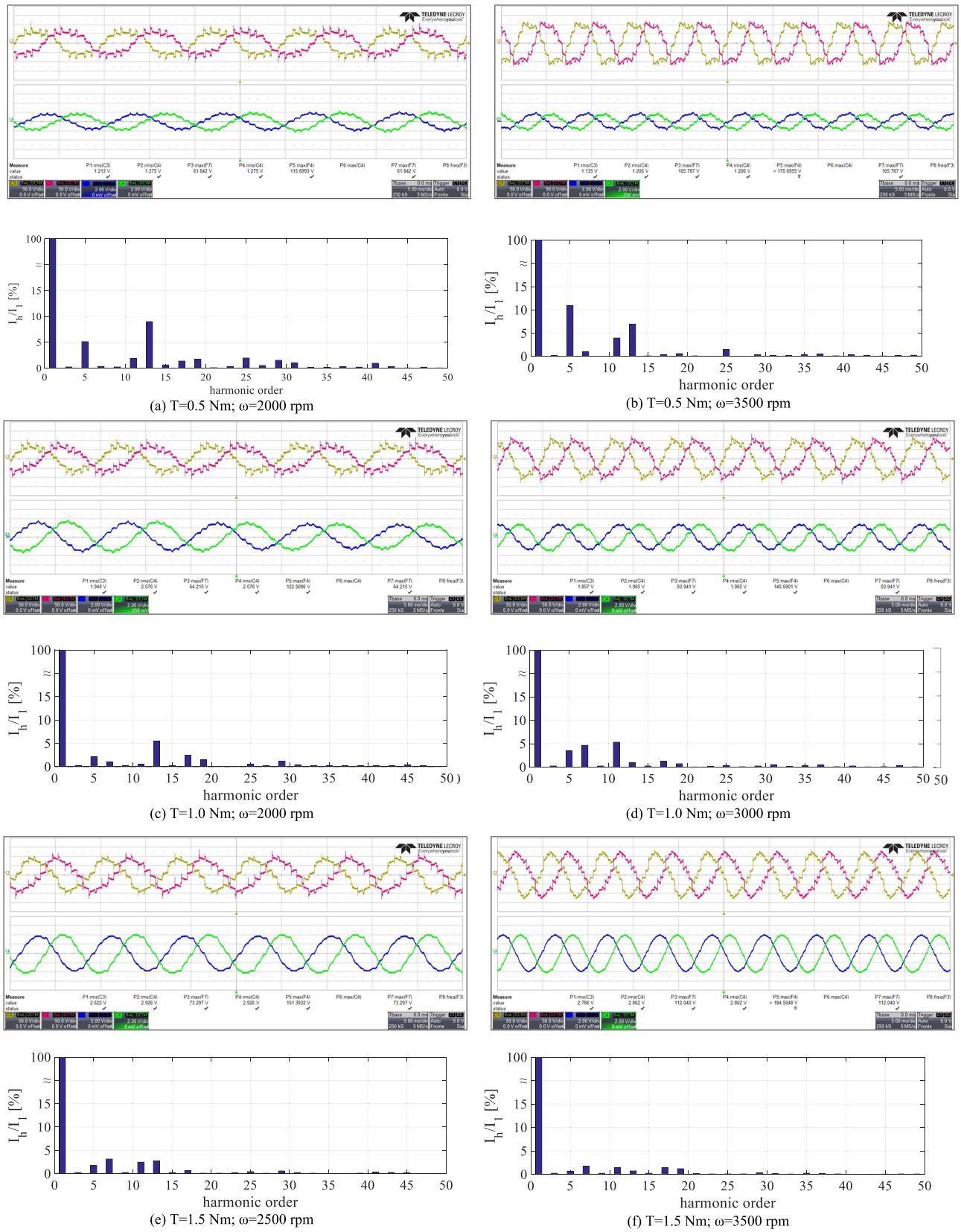

(a) T=0.5 Nm; ω=2000 rpm

(b) T=0.5 Nm; ω=3500 rpm

(c) T=1.0 Nm; ω=2000 rpm

(d) T=1.0 Nm; ω=3000 rpm

(e) T=1.5 Nm; ω=2500 rpm

(f) T=1.5 Nm; ω=3500 rpm

FIGURE 30. Experimental voltages (yellow and red curves), currents (green and blue curves) of phase *a* and *b* of the motor for some working points and corresponding current harmonic spectra.

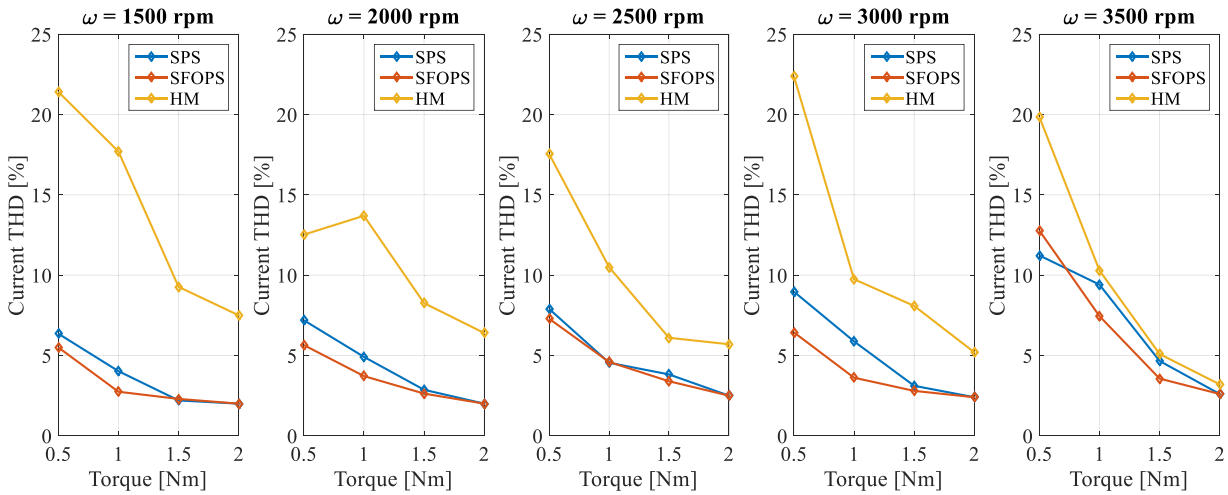

FIGURE 31. Experimental comparison of current THD%.

Regarding the motor efficiency, in almost all IPMSM working points, the motor performance, obtained with HM modulation strategy, are higher with respect to the motor performance, obtained with the SFOPS modulation strategy. In detail, an improvement of up to about 1.5% in the motor efficiency with the HM modulation strategy has been detected with respect to the motor efficiency obtained with the SFOPS modulation strategy. Furthermore, the motor efficiency trend detected with HM modulation strategy is comparable with respect to the motor efficiency trend detected with SPS modulation strategy only for low mechanical load, or rather load torque equal to 0.5 Nm and mechanical speed equal to 1500 rpm and 2000 rpm. In this case, an improvement of up to about 1.2% in the efficiency with the HM modulation strategy has been detected. The efficiency improvement detected, due to the HM algorithm operations, is due to a substantial reduction in iron losses since the fifth, seventh and eleventh voltage harmonic components are mitigated and the high-frequency voltage harmonic components are absent. Copper losses are a function of the absorbed current or the applied load torque and, therefore, do not affect the motor efficiency as the modulation technique used varies.

Regarding the overall drive efficiency, in all IPMSM working points, the drive performance are significantly better by the use of HM modulation strategy with respect to those obtained with SFO and SPS modulation strategies. In detail, improvements in drive efficiency greater than 2% have been identified by the use of HM modulation strategy. This behaviour can be attributed to the CHBMI efficiency improvement which, when calculating the efficiency of the drive, amplifies the efficiency gain obtained on the motor. The results obtained confirm the analysis carried out in a simulation environment.

Another quantity of interest in these experimental investigations is the torque ripple which, unfortunately, could not be estimated directly because the torque sensor of the Magtrol hysteresis brake presents a limited frequency bandwidth. However, the torque ripple is a function of the current harmonic components and, therefore, the latter have been investigated and analyzed. Some acquisitions performed during the experimental investigations with the Oscilloscope Teledyne Lecroy 640Zi and the relative current frequency spectrum are reported in Fig. 30 when the IPMSM is driven by the HM modulation strategy. In detail, the fifth, seventh, eleventh and thirteenth current harmonic components present not negligible amplitude, especially for low load torque. In particular, for low mechanical load values, mechanical speed less than 1000 rpm and torque loads less than or equal to 0.5 Nm, the torque oscillations present generate audible vibrations. For higher mechanical loads, significant and audible vibrations were not detected, resulting comparable to those generated by the SPS and SFO modulation strategies. This result can also be deduced from the analysis of the current THDs reported in Fig. 31. In this analysis, the difference in amplitude between current THD values obtained by the use of HM modulation strategy and current THD values obtained with the other two modulation strategies is higher for low mechanical loads. Whereas, for high mechanical load values, this difference is significantly reduced. This analysis is also in agreement with the results obtained from the analysis carried out in a simulation environment.

VII. CONCLUSION

In this article, an evaluation impact of HM on IPMSM drive performance, fed by CHBMI, has been proposed and investigated. For this purpose, other two traditional pulse width modulation (PWM) strategies, sinusoidal phase-shifted (SPS) and Switching frequency optimal phase-shifted (SFOPS) have been considered and used for comparison analysis. In detail, the performance analysis of the IPMSM drive has been carried out first in a simulation environment through the use of an enhanced modelling approach of IPMSM and subsequently through experimental investigations. The comparison has been carried out by a field-oriented control of low power

IPMSM, and, the electric drive overall efficiency, torque ripple, voltage and current THD have been evaluated for each modulation strategy. The study conducted has shown an increase in the IPMSM drive overall efficiency by the use of the proposed HM with respect to the other two modulation strategies (even greater than 2% in some work points). The increase in the IPMSM drive overall efficiency obtained by the use of HM is justified by the voltage THD or the harmonic content of the supply voltages that result in iron losses and converter losses reduction. Instead, better IPMSM drive performance in terms of torque ripple has been detected by the use of traditional PWM strategies that respect the proposed HM, especially for low speed and load torque values, far from nominal values. Comparable results in terms of torque ripple have been obtained for high speed and load torque values. This result can also be detected in the current harmonic analysis or current THD trend. Although the use of IPMSM drive fed by CHBMI presents several advantages in terms of control flexibility, modular structure, electrical safety, the use of the proposed HM allows obtaining promising results in terms IPMSM drive overall efficiency increase, which is very interesting for transportation applications where efficiency is a crucial parameter for increase the travel autonomy.

REFERENCES

[1] A. I. Elsanabary, G. Konstantinou, S. Mekhilef, C. D. Townsend, M. Seyedmahmoudian, and A. Stojcevski, "Medium voltage large-scale grid-connected photovoltaic systems using cascaded H-bridge and modular multilevel converters: A review," *IEEE Access*, vol. 8, pp. 223686–223699, 2020, doi: 10.1109/ACCESS.2020.3044882.

[2] S. Debnath, J. Qin, B. Bahrani, M. Saeedifard, and P. Barbosa, "Operation, control, and applications of the modular multilevel converter: A review," *IEEE Trans. Power Electron.*, vol. 30, no. 1, pp. 37–53, Jan. 2015.

[3] Y. Yu, G. Konstantinou, B. Hredzak, and V. G. Agelidis, "Power balance optimization of cascaded H-Bridge multilevel converters for large-scale photovoltaic integration," *IEEE Trans. Power Electron.*, vol. 31, no. 2, pp. 1108–1120, Feb. 2016.

[4] T. H. Nguyen, K. A. Hosani, M. S. E. Moursi, and F. Blaabjerg, "An overview of modular multilevel converters in HVDC transmission systems with STATCOM operation during pole-to-pole DC short circuits," *IEEE Trans. Power Electron.*, vol. 34, no. 5, pp. 4137–4160, May 2019.

[5] B. S. Umesh and K. Sivakumar, "Multilevel inverter scheme for performance improvement of pole-phase-modulated multiphase induction motor drive," *IEEE Trans. Ind. Electron.*, vol. 63, no. 4, pp. 2036–2043, Apr. 2016.

[6] D. Mohan, X. Zhang, and G. H. Beng Foo, "Generalized DTC strategy for multilevel inverter fed IPMSMs with constant inverter switching frequency and reduced torque ripples," *IEEE Trans. Energy Convers.*, vol. 32, no. 3, pp. 1031–1041, Sep. 2017.

[7] L. Liu, H. Li, S. Hwang, and J. Kim, "An energy-efficient motor drive with autonomous power regenerative control system based on cascaded multilevel inverters and segmented energy storage," *IEEE Trans. Ind. Appl.*, vol. 49, no. 1, pp. 178–188, Jan./Feb. 2013.

[8] A. R. Beig and A. Dekka, "Experimental verification of multilevel inverter-based standalone power supply for low-voltage and low-power applications," *IET Power Electron.*, vol. 5, no. 6, pp. 635–643, Jul. 2012.

[9] M.H. Rashid, *Power Electronics: Devices, Circuits and Applications*, 4th Ed. Pearson India.

[10] S. G. Min and B. Sarlioglu, "Modeling and investigation on electromagnetic noise in PM motors with single- and double-layer concentrated winding for EV and HEV application," *IEEE Trans. Transp. Electrific.*, vol. 4, no. 1, pp. 292–302, Mar. 2018.

[11] J. Liang, A. Parsapour, Z. Yang, C. Caicedo-Narvaez, M. Moallem, and B. Fahimi, "Optimization of air-gap profile in interior permanent-magnet synchronous motors for torque ripple mitigation," *IEEE Trans. Transp. Electrific.*, vol. 5, no. 1, pp. 118–125, Mar. 2019.

[12] G. Pellegrino, A. Vagati, P. Guglielmi, and B. Boazzo, "Performance comparison between surface-mounted and interior PM motor drives for electric vehicle application," *IEEE Trans. Ind. Electron.*, vol. 59, no. 2, pp. 803–811, Feb. 2012.

[13] Z. Yang, F. Shang, I. P. Brown, and M. Krishnamurthy, "Comparative study of interior permanent magnet, induction, and switched reluctance motor drives for EV and HEV applications," *IEEE Trans. Transp. Electrific.*, vol. 1, no. 3, pp. 245–254, Oct. 2015.

[14] S. Wu, C. Tian, W. Zhao, J. Zhou, and X. Zhang, "Design and analysis of an integrated modular motor drive for more electric aircraft," *IEEE Trans. Transp. Electrific.*, vol. 6, no. 4, pp. 1412–1420, Dec. 2020.

[15] R. Pothuraju, T. Ramesh, and P. D. Kumar, "DTFC-SVM based Five-level cascaded inverter with reduced switches fed interior type permanent magnet synchronous motor drive," in *Proc. IEEE 9th Power India Int. Conf.*, 2020, pp. 1–6.

[16] D. Mohan, X. Zhang, and G. H. B. Foo, "Three-Level inverter-fed direct torque control of IPMSM with constant switching frequency and torque ripple reduction," *IEEE Trans. Ind. Electron.*, vol. 63, no. 12, pp. 7908–7918, Dec. 2016.

[17] V. Yaramasu and B. Wu, "Predictive control of a three-level boost converter and an NPC inverter for high-power PMSG-Based medium voltage wind energy conversion systems," *IEEE Trans. Power Electron.*, vol. 29, no. 10, pp. 5308–5322, Oct. 2014,.

[18] R. Baidya, R. P. Aguilera, P. Acuña, S. Vazquez, and H. D. T. Mouton, "Multistep model predictive control for cascaded H-bridge inverters: Formulation and analysis," *IEEE Trans. Power Electron.*, vol. 33, no. 1, pp. 876–886, Jan. 2018.

[19] H. Yao, Y. Yan, T. Shi, G. Zhang, Z. Wang, and C. Xia, "A novel SVPWM scheme for field oriented vector controlled PMSM drive system fed by cascaded H-bridge inverter," *IEEE Trans. Power Electron.*, vol. 36, no. 8, pp. 8988–9000, Aug. 2021, doi: 10.1109/TPEL.2021.3054642.

[20] A. Poorfakhraei, M. Narimani, and A. Emadi, "A review of modulation and control techniques for multilevel inverters in traction applications," *IEEE Access*, vol. 9, pp. 24187–24204, 2021.

[21] M. S. A. Dahidah, G. Konstantinou, and V. G. Agelidis, "A review of multilevel selective harmonic elimination PWM: Formulations, solving algorithms, implementation, and applications," *IEEE Trans. Power Electron.*, vol. 30, no. 8, pp. 4091–4106, Aug. 2015.

[22] W. Yao, H. Hu, and Z. Lu, "Comparisons of space-vector modulation and carrier-based modulation of multilevel inverter," *IEEE Trans. Power Electron.*, vol. 23, no. 1, pp. 45–51, Jan. 2008.

[23] A. Edpuganti and A. K. Rathore, "A survey of low switching frequency modulation techniques for medium-voltage multilevel converters," *IEEE Trans. Ind. Appl.*, vol. 51, no. 5, pp. 4212–4228, Sep./Oct. 2015.

[24] S. Kouro *et al.*, "Recent advances and industrial applications of multilevel converters," *IEEE Trans. Ind. Electron.*, vol. 57, no. 8, pp. 2553–2580, Aug. 2010.

[25] J. N. Chiasson, L. M. Tolbert, K. J. McKenzie, and Zhong Du, "A unified approach to solving the harmonic elimination equations in multilevel converters," *IEEE Trans. Power Electron.*, vol. 19, no. 2, pp. 478–490, Mar. 2004.

[26] K. Yang *et al.*, "Unified selective harmonic elimination for multilevel converters," *IEEE Trans. Power Electron.*, vol. 32, no. 2, pp. 1579–1590, Feb. 2017.

[27] C. Buccella, C. Cecati, M. G. Cimoroni, and K. Razi, "Analytical method for pattern generation in five-level cascaded H-Bridge inverter using selective harmonic elimination," *IEEE Trans. Ind. Electron.*, vol. 61, no. 11, pp. 5811–5819, Nov. 2014.

[28] C. Buccella, C. Cecati, M. G. Cimoroni, G. Kulothungan, A. Edpuganti, and A. K. Rathore, "A selective harmonic elimination method for five-level converters for distributed generation," *IEEE J. Emerg. Sel. Topics Power Electron.*, vol. 5, no. 2, pp. 775–783, Jun. 2017.

[29] G. Schettino, F. Viola, A. O. Di Tommaso, P. Livreri, and R. Miceli, "Experimental validation of a novel method for harmonic mitigation for a three-phase five-level cascaded H-bridges inverter," *IEEE Trans. Ind. Appl.*, vol. 55, no. 6, pp. 6089–6101, Nov./Dec. 2019.

[30] A. Tripathi and G. Narayanan, "Evaluation and minimization of low-order harmonic torque in low-switching-frequency inverter-fed induction motor drives," *IEEE Trans. Ind. Appl.*, vol. 52, no. 2, pp. 1477–1488, Mar./Apr. 2016.
[31] G. Nalcaci, D. Yildirim, and M. Ermis, "Selective harmonic elimination for light-rail transportation motor drives using harris hawks algorithm," in *Proc. IEEE Int. Conf. Environ. Elect. Eng. 2020 IEEE Ind. Commercial Power Syst. Europe*, 2020, pp. 1–6.
[32] Y. Liang, D. Liang, S. Jia, S. Chu, and J. He, "A full-speed range hybrid PWM strategy for high-speed permanent magnet synchronous machine considering mitigation of current harmonics," in *Proc. IEEE Energy Convers. Congr. Expo.*, 2019, pp. 1886–1890.
[33] M. P. Brito Gomes, M. Hassen de Souza, G. V. Ramos, A. A. Luiz, and M. M. Stopa, "Application of a SHE-PWM modulation for a low switching frequency motor drive with harmonic investigation using the DTFT," in *Proc. IEEE 15th Braz. Power Electron. Conf. 5th IEEE Southern Power Electron. Conf.*, 2019, pp. 1–6.
[34] G. S. Lakshmi, P. V. Kumar, and P. Sudeepika, "Field oriented control of IPMSM using diode-clamped multilevel inverter," in *Proc. Int. Conf. Power Adv. Control Eng.*, 2015, pp. 355–360.
[35] G. S. Lakshmi, "Performance analysis of multi-level diode-clamped inverter fed IPMSM drive for electric vehicles," in *Proc. IEEE Innov. Smart Grid Technol. Asia*, 2018, pp. 54–61.
[36] S. Lakshmi Gundebommu, "Five-level and seven-level DCMI fed to IPMSM," in *Proc. Int. Conf. Elect. Eng. Res. Pract.*, 2019, pp. 1–6.
[37] V. Patel, M. Tinari, C. Buccella, and C. Cecati, "Analysis on multilevel inverter powertrains for E-transportation," in *Proc. IEEE 13th Int. Conf. Compat., Power Electron. Power Eng.*, 2019, pp. 1–6.
[38] V. Patel, C. Buccella, A. M. Saif, M. Tinari, and C. Cecati, "Performance comparison of multilevel inverters for E-transportation," in *Proc. Int. Conf. Elect. Electron. Technol. for Automot.*, 2018, pp. 1–6.
[39] Vidhi Patel, Concettina Buccella, and Carlo Cecati, "Analysis and implementation of multilevel inverter for full electric aircraft drives," *Energies*, vol. 13, no. 22, 2020, Art. no. 6126.
[40] X. Chen, J. Wang, B. Sen, P. Lazari, and T. Sun, "A high-fidelity and computationally efficient model for interior permanent-magnet machines considering the magnetic saturation, spatial harmonics, and iron loss effect," *IEEE Trans. Ind. Electron.*, vol. 62, no. 7, pp. 4044–4055, Jul. 2015.
[41] X. Chen, J. Wang, and A. Griffo, "A high-fidelity and computationally efficient electrothermally coupled model for interior permanent-magnet machines in electric vehicle traction applications," *IEEE Trans. Transp. Electrific.*, vol. 1, no. 4, pp. 336–347, Dec. 2015.
[42] A. Rabiei, T. Thiringer, M. Alatalo, and E. A. Grunditz, "Improved maximum-torque-per-ampere algorithm accounting for core saturation, cross-coupling effect, and temperature for a PMSM intended for vehicular applications," *IEEE Trans. Transp. Electrific.*, vol. 2, no. 2, pp. 150–159, Jun. 2016.
[43] A. Gebregergis, M. H. Chowdhury, M. S. Islam, and T. Sebastian, "Modeling of permanent-magnet synchronous machine including torque ripple effects," *IEEE Trans. Ind. Appl.*, vol. 51, no. 1, pp. 232–239, Jan./Feb. 2015.
[44] N. Bianchi and L. Alberti, "MMF harmonics effect on the embedded FE analytical computation of PM motors," *IEEE Trans. Ind. Appl.*, vol. 46, no. 2, pp. 812–820, Mar./Apr. 2010.
[45] S. Li, D. Han, and B. Sarlioglu, "Modeling of interior permanent magnet machine considering saturation, cross-coupling, spatial harmonics, and temperature effects," *IEEE Trans. Transp. Electrific.*, vol. 3, no. 3, pp. 682–693, Sep. 2017.
[46] A. Dietz, M. Caruso, A. O. Di Tommaso, R. Miceli, and C. Nevoloso, "Enhanced mathematical modelling of interior permanent magnet synchronous machine considering saturation, cross-coupling and spatial harmonics effects," in *Proc. Fifteenth Int. Conf. Ecological Veh. Renewable Energies*, 2020, pp. 1–9.
[47] G. Ala *et al.*, "Experimental investigation on the performances of a multilevel inverter using a field programmable gate array-based control system," *Energies*, vol. 12, no. 6, 2019, Art. no. 1016.
[48] G. Holmes and T.A. Lipo *Pulse Width Modulation For Power Converters: Principle and Practice*. Piscataway, NJ, USA: IEEE Press, 2003.
[49] G. Feng, C. Lai, and N. C. Kar, "Practical testing solutions to optimal stator harmonic current design for PMSM torque ripple minimization using speed harmonics," *IEEE Trans. Power Electron.*, vol. 33, no. 6, pp. 5181–5191, Jun. 2018.

GIUSEPPE SCHETTINO received the bachelor's and the master's degree in electrical engineering from the University of Palermo, Italy, in 2012 and 2015, respectively. In 2018 he received the Ph.D degree in energy and information technologies at the same university whit the Ph.D thesis "Cascaded H-Bridges multilevel inverter: grid connected advanced applications". Dr. Schettino is currently doing post doc research at the Department of Engineering of the same university. He is co-author of more 65 papers published in international conference proceedings and journals. His research activity regards the multilevel power converters, modulation techniques and control strategies for grid connected and electrical drives applications.

CLAUDIO NEVOLOSO received the M.S. and Ph.D. degrees in electrical engineering from the University of Palermo, Palermo, Italy, in 2016 and 2020, respectively. He is currently a Postdoctoral Researcher with Sustainable Development and Energy Saving Laboratory, University of Palermo. His main research interests include the design, mathematical modelling, and characterization of electrical machines and drives.

ROSARIO MICELI (Member, IEEE) received the B.S. degree and the Ph.D. degree in electrical engineering from the University of Palermo, Palermo, Italy, in 1982 and 1987, respectively. He is currently a Full Professor of electrical machines with Polytechnic School, University of Palermo, where he is also a Personnel in Charge with the Sustainable Development and Energy Savings Laboratory. His main research interests include mathematical models of electrical machines, drive system control, and diagnostics, renewable energies, and energy management. Prof. Miceli is a Reviewer for the IEEE TRANSACTIONS ON INDUSTRIAL ELECTRONICS and the IEEE TRANSACTIONS ON INDUSTRY APPLICATIONS.

ANTONINO OSCAR DI TOMMASO was born in Tbingen, Germany, on June 5, 1972. He received the master's and Ph.D. degrees in electrical engineering from the University of Palermo, Palermo, Italy, in 1999 and 2004, respectively. He was a Post Ph.D. Fellow of electrical machines and drives, from 2004 to 2006, and Researcher, from 2006 to 2019, with the Department of Electrical Engineering, University of Palermo, where he is currently an Associate Professor of electrical machines and drives with the Department of Engineering. His research interests include electrical machines, drives, diagnostics on power converters, and diagnostics and design of electrical machines.

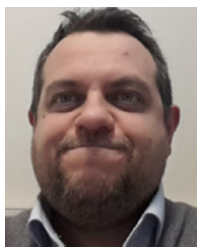

FABIO VIOLA (Member, IEEE) received the M.Sc. and Ph.D. degrees in electrical engineering from the University of Palermo, Palermo, Italy, in 2002 and 2006, respectively. In 2008, he joined the Department of Electrical, Electronic, and Telecommunication Engineering, University of Palermo, as a Researcher. Since the same year, he holds the basic electrical engineering course. His research interests include the field of electromagnetic compatibility, high voltage, partial discharges diagnosis, renewable energy, electric vehicles, power electronic converters, and energy harvesting.